Lipase-mediated selective hydrolysis of lipid droplets in phase separated-liposomes

*Panagiota Papadopoulou[1#], Rianne van der Pol[1#], Niek van Hilten[1#], Mohammad-Amin Moradi[2], Maria J. Ferraz[3], Johannes M.F.G. Aerts[3], H. Jelger Risselada[1,4,5], G.J. Agur Sevink[6], Alexander Kros[1]**

[1]Department of Supramolecular & Biomaterials Chemistry, Leiden Institute of Chemistry (LIC), Leiden University, P.O. Box 9502, 2300 RA Leiden, The Netherlands.

[2]Department of Chemical Engineering and Chemistry, Eindhoven University of Technology, P.O. Box 513, 5600 MB, Eindhoven, The Netherlands.

[3]Department of Medical Biochemistry, Leiden Institute of Chemistry (LIC), Leiden University, P.O. Box 9502, 2300 RA Leiden, The Netherlands.

[4]Department of Physics, Technical University Dortmund, Dortmund 44221, Germany

[5]Institute for Theoretical Physics, Georg-August-University Göttingen, Göttingen 37077, Germany

[6]Department of Biophysical Organic Chemistry, Leiden Institute of Chemistry (LIC), Leiden University, P.O. Box 9502, 2300 RA Leiden, The Netherlands.

[#]Authors contributed equally.
*E-mail: a.kros@chem.leidenuniv.nl

ABSTRACT

The membrane-protein interface in lipid nanoparticles (LNPs) is important for their in vivo behavior. Better understanding may assist to evolve current drug delivery methods to more precise, cell- or tissue-specific nanomedicine. Previously, we demonstrated how phase separation can drive liposomes to cell specific accumulation *in vivo*, through the selective recognition of phase-separated liposomes by triacylglycerol lipases (TGLs). This exemplified how liposome morphology can determine the preferential interaction of nanoparticles with biologically relevant proteins. Here, we investigate in detail the lipase-induced morphological changes of phase separated liposomes - which bear a lipid droplet in their bilayer - and unravel how lipase recognizes and binds to the particles at a molecular level. We find that phase separated liposomes undergo selective lipolytic degradation of their lipid droplet while overall nanoparticle integrity remains intact. Next, we combined MD simulations and *in vitro* experiments to identify the Tryptophan-rich loop of the lipase – a region which is involved endogenously in lipoprotein binding – as the region through which the enzyme binds to the particle. We demonstrate that this preferential binding is due to the lipid packing defects induced on the membrane by phase separation. These findings are a significant example of selective LNP – protein communication and interaction, aspects that may further the control of the *in vivo* behavior of lipid nanoparticles.

INTRODUCTION

Lipid-based nanomedicine is undoubtably a research field of growing importance. Various liposomal drug formulations have been marketed and used in the clinic over the last decades.[1] More recently, the development of RNA-based lipid nanoparticles has shown great potential, paving the way for future innovations.[2–6] To push this technology forward, towards simpler, yet more efficient and tissue specific formulations for drug delivery, there is a need for a greater understanding of the *in vivo* behavior of such lipid nanoparticles (LNPs). A key step is to study the interactions of LNPs with biologically relevant proteins at the nano-bio interface, since it is well known that such interactions i.e., lead to the formation of a protein corona, which can determine the *in vivo* fate of LNPs to a great extent[7–10] ; or they can lead to preferential protein binding or induce morphological changes in the membrane and affect the supramolecular assembly[11,12], which in turn could also affect their *in vivo* fate.

Previously[13], in a liposome screening study in zebrafish embryos, a novel formulation (named PAP3) was found to selectively interact with (capillary) lumen-bound triglyceride lipases (TGLs), enzymes involved in lipid transport and metabolism. The interaction led to the selective accumulation of PAP3 liposomes in (endothelial) cell subsets rich in TGLs. Liposome-lipase interactions are mediated solely through a unique phase-separated LNP morphology, in which liposomes bare a single lipid droplet in each bilayer (**Figure 1a**). This aspect was found to be the key element for the specific accumulation and for interaction with TGLs. This is, to our knowledge, the first time that phase-separation is used to target specific cells *in vivo*. PAP3 liposomes consist of an equimolar mixture of 1,2-distearyl-*sn*-glycero-3-phosphatidylcholine (DSPC) – a naturally occurring phospholipid – and 2-hydroxy-3-oleamidopropyl-oleate (DOaG), a synthetic lipid structurally analogous to the monounsaturated diacylglycerol, dioleoylglycerol (DOG) (**Figure 1b**). Diacylglycerols (DAGs) are endogenous signaling lipids and their local accumulation in the cell membrane induces morphological changes, which in turn orchestrate signaling, *e.g.,* activation of Protein Kinase C (PKC) or Phospholipase C.[14–16] Their conical shape, attributed to the small polar hydroxyl group and bulky fatty acid tails, is associated with negative curvature. When added to phospholipid membranes, they are known to perturb lamellar bilayers and even induce phase separation and formation of non-bilayer phases (i.e., lipid droplets) above a threshold (miscibility) concentration.[17,18] Our particular liposomal formulation follows the same principles and is a great example of how DAG analogues can generate a lipid droplet by their local accumulation between the DSPC leaflets. Another important aspect of DAGs is that they increase the spacing between adjacent phospholipid headgroups in a lipid membrane, even below the threshold concentration, an effect that is amplified by curvature.[19] The transient domains that form as a consequence of such packing frustrations and transiently expose the apolar domain of the lipid membrane, are known as lipid packing defects.[18,20–22] Some membrane peripheral proteins have been proposed to rely on these hydrophobic lipid packing defects - caused by factors such as phase separation, lateral tension, or membrane curvature - for membrane binding and activation.[23,24] Examples include the Golgi-associated protein ArfGAP1, that senses curvature-induced packing defects through an amphipathic lipid packing sensor motif [25,26] and the CTP:phosphocholine cytidylyltransferase (CCT), that binds to large packing defects on lipid droplets.[27] Also, the toxin Equinatoxin-II[28] and several lipases[29,30] have been found to sense packing defects, induced by DAGs in particular.

Triglyceride lipases (TGLs) are lipolytic enzymes bound at the luminal surface of capillaries, and are involved in lipid transport and metabolism, primarily through their interaction with freely circulating lipoproteins. They either hydrolyze tri- and di-acylglycerols and cholesteryl esters or phospholipids, remodeling lipoprotein particles and promoting influx of fatty acids into the cell; or they act as bridging molecules to facilitate lipoprotein uptake.[31,32] The family consists mainly of hepatic lipase (HL)[33], lipoprotein lipase (LPL)[34] and endothelial lipase (EL).[35] The main functional domains – the lipid binding domain for substrate binding, the lid region containing the catalytic triad of Serine (Ser), Aspartate (Asp), Histidine (His) and the heparin binding domain - are all structurally homologous throughout the lipase protein family (see [36,37] and **Figure S23** for protein alignment). The lipid binding domain is rich in hydrophobic residues, mainly tryptophans (Trp), forming a hydrophobic Trp-rich loop that is responsible for insertion of the protein in the hydrophobic lipid core of lipoproteins.[33,38–41] Importantly, lipases have been found to depend on lipids on the lipoprotein membrane, but not apolipoproteins, for binding.[42]

Therefore, in this study, we combine experimental characterization and (coarse-grained) molecular dynamics (MD) simulations to investigate the molecular mechanism through which the TGL lipoprotein lipase (LPL) interacts with the PAP3 phase-separated liposomes and the subsequent morphological changes of the liposomes upon incubation. First, by combining morphological liposome analysis by Cryo-Transmission Electron Microscopy (Cryo-TEM) with enzymatic activity analysis of LPL, we observe selective lipolytic degradation of the lipid droplet of PAP3 liposomes (rich in DOaG), while the overall nanoparticle integrity and structure is maintained. Mass spectrometry analysis confirms the selective hydrolysis of DOaG over DSPC, consistent with the known preference of LPL for hydrolyzing Tri- and Di-acylglycerols. Next, we built upon earlier insight in the role of defects for protein binding [23,24] and study lipid packing defects in PAP3 liposomes and their role in recognition and binding of LPL. By combining Cryo-TEM with molecular dynamics (MD) simulations we confirm and quantify increased packing defects on the curved DSPC monolayer surrounding the DOaG lipid droplet, leading to the insight that (induced) curvature and DOaG availability are the two likely ingredients for selective LPL binding. Finally, free energy calculations and enzymatic activity analysis reveal that the Trp-rich loop of LPL acts as a lipid packing defect sensing motif, that prefers to interact with a PAP3 membrane (DSPC/DOaG) over the (flat) pure DSPC counterpart.

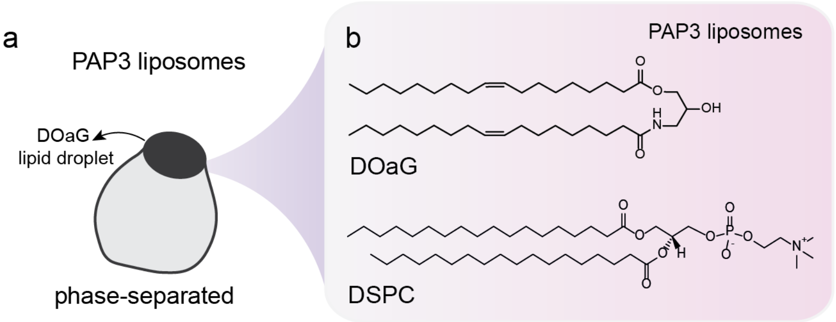

Figure 1. Molecular details of PAP3 liposomes. a) Schematic representation of phase separated liposomes (named PAP3). **b)** Molecular structures of DOaG and DSPC combined in an equimolar mixture (50:50) to form PAP3 liposomes.

RESULTS

DOaG lipid droplet selectively depleted by Lipoprotein Lipase

To determine any morphological changes on PAP3 liposomes upon incubation with a TGL, the phase separated liposomes were incubated with LPL at physiological conditions (pH = 7.4, 37°C) for 3 h and changes in the morphology were assessed by Cryo-TEM imaging (**Figure 2a**). As expected without addition of LPL, nearly 80 % of PAP3 liposomes incubating at 37 °C for 3 h were phase separated (**Figure 2b-d** and **Figure S1a**) with only ~20 % of the population having another morphology, either (multi-) lamellar, solid-lipid or unidentifiable. Strikingly, when PAP3 liposomes were incubated with LPL, liposomes were now lacking the lipid droplet (**Figure 2e** and **Figure S1b**), and less than 10 % of the population appeared now to be phase separated (**Figure 2f, g**), with almost 80 % of the population being now lamellar. This indicated that LPL could deplete the phase separated droplet possibly through its lipolytic activity, therefore selectively hydrolyzing the DOaG lipid. Accordingly, when the denatured and therefore inactive form of LPL was added to the PAP3 liposomes, no change of the phase separated morphology or the percentage in the population was observed (**Figure 2h-j** and **Figure S1c**), implying the catalytically active LPL to be responsible for the selective droplet digestion. Interestingly, despite the major morphological change on PAP3 liposomes, the nanoparticles remained intact in terms of structural integrity, retaining their size of about 120 nm over time (**Figure S2** and **table S1**). Of note, liposomes without DOaG, (i.e., 100 % DSPC), did not display any changes in morphology or size before and after addition of LPL (**Figure S3** and **table S1**) suggesting no interaction, and as before signifying that LPL is selective for DOaG or the phase separation induced by DOaG.

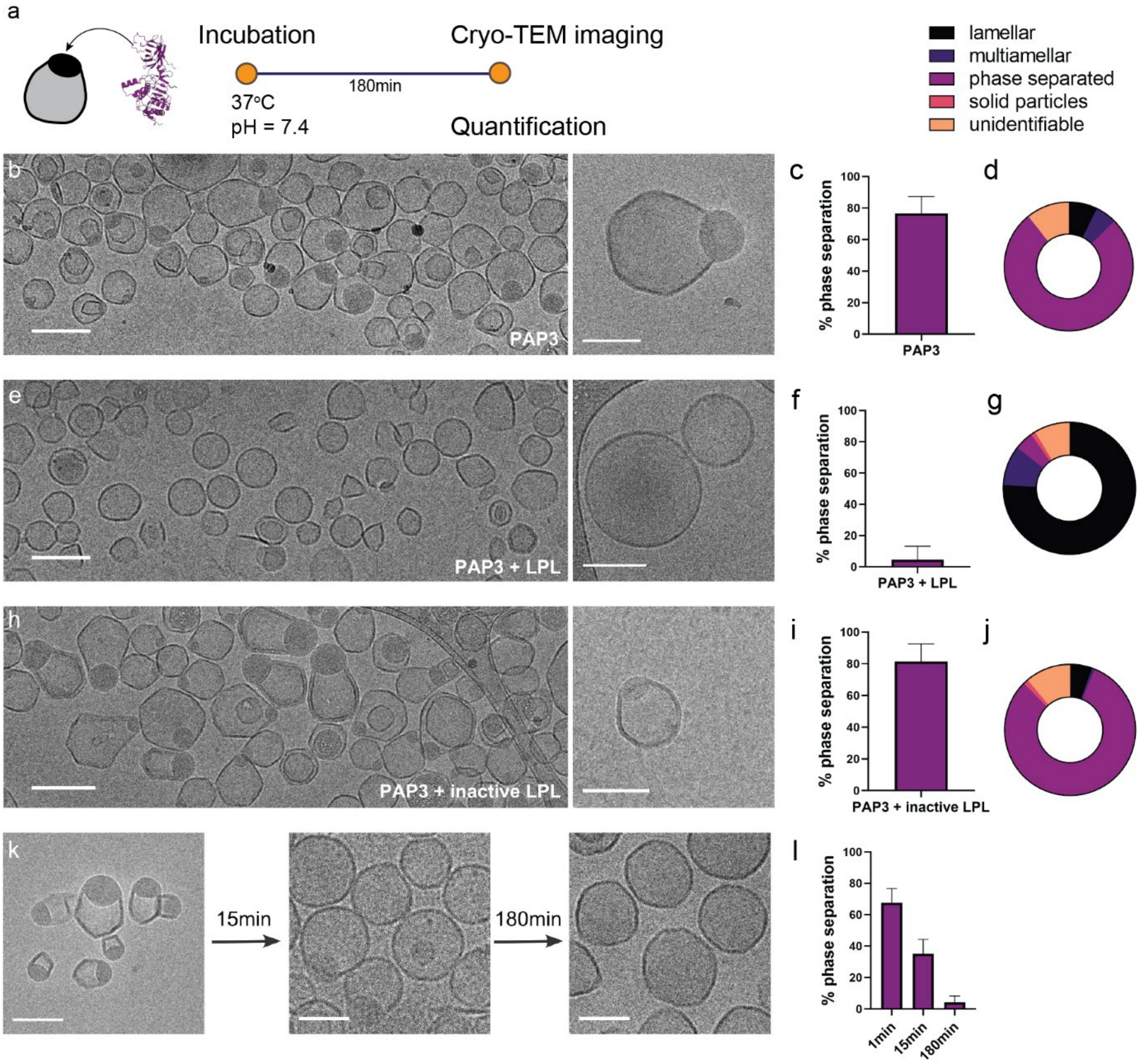

Figure 2. Selective depletion of DOaG lipid droplets in PAP3 liposomes. a) Schematic for conditions and timeline of cryo-TEM imaging. **b)** Low and high magnification cryo-TEM images depicting PAP3 liposomes at 37 ºC incubating for 180 min. **c)** Percentage of phase separation on PAP3 liposomes based on cryo-TEM quantification (N=200) and **d)** Quantification of all populations found on PAP3 liposomal formulation incubating at 37 ºC for 180 min. **e)** Low and high magnification cryo-TEM images depicting PAP3 liposomes incubating with LPL for 180 min. **f)** Percentage of phase separation on PAP3 liposomes based on cryo-TEM quantification (N=200) and **g)** Quantification of all populations found on the formulation after incubation with LPL for 180 min. **h)** Low and high magnification cryo-TEM images depicting PAP3 liposomes incubating with inactive LPL for 180 min. **i)** Percentage of phase separation on PAP3 liposomes based on cryo-TEM quantification (N=200) and **j)** Quantification of all populations found on the formulation after incubation with inactive LPL for 180 min. **k)** Cryo-TEM images of PAP3 liposomes incubating with LPL for 1, 15 and 180 min. **l)** Percentage of phase separation on PAP3 liposomes based on cryo-TEM quantification (N=200) after incubation with LPL for 1, 15 and 180 min. Scale bars: 200 nm for b, e, h and 100 nm for k and insets on b, e, h.

LPL selectively hydrolyzes DOaG but not DSPC

Subsequently, to assess the evolution and timeline of the observed morphological change, PAP3 liposomes were imaged after incubating for 1, 15 and 180 min with LPL and the percentage of phase separation was found to progressively decrease over time (**Figure 2k-l** and **Figure S4**). This indicated that the observed phenomenon was a dynamic process, and that lipolysis could be monitored overtime by quantifying the amount of free fatty acids (FFA),[43,44] released as metabolite products from the hydrolysis of the co-formulants DOaG and/or DSPC (**Figure 3a**). For this, a non-esterified free fatty acid measurement kit (NEFA-kit) was used, along with mass spectrometry which was used to determine which lipid is preferentially hydrolyzed (**Figure 3b**). As expected, PAP3 liposomes incubated with LPL released ~0.9 mmoL/L of FFA over a period of 300 min (**Figure 3c**) and hydrolysis continued beyond this point (**Figure S5**). Incubation of PAP3 liposomes without LPL, or incubation of PAP3 liposomes with inactivated LPL, as well as incubation of 100% DPSC liposomes with LPL, did not release any significant amount of FFA over the same period, again indicating the specificity of LPL for DOaG in mixed and/or phase separated membranes (**Figure 3c**). Here, to also verify the LPL preference on naturally occurring DAGs - along with DOaG as a DAG analogue - we formulated phase-separated liposomes consisting of DOG and DSPC. Subsequently, we monitored the FFA release and structural changes of the DSPC/DOG liposomes upon LPL incubation (**Figure S6**). The results showed similar preference of LPL on DOG-containing liposomes as on PAP3. Similarly, to assess the influence of LPL on liposomes that are known to freely circulate *in vivo* and not particularly interact with cells types and proteins,[8] a formulation based on the clinically approved Myocet®[45] (composition: POPC:CHO_55:45) was also incubated at 37 °C with LPL for 180 min, which did not result in FFA release, indicating no interaction with LPL (**Figure S7**). Next, mass spectrometry analysis was used to investigate the hydrolysis of the lipids in the PAP3 formulation. The DOaG/DSPC ratio was measured before and after addition of LPL, indicating a decrease only for the DOaG lipid after addition of LPL and signifying that 30.7% of DOaG was hydrolyzed (**Figure 3d** and **Figure S8**). Given that DOaG is the only lipid hydrolyzed, FFA was again measured immediately after the mass spectrometry and found to correspond to 31% of hydrolyzed DOaG, in agreement with the mass spectrometry value (**Figure 3e**). In our previous studies[13], lipase-mediated uptake of PAP3 liposomes was inhibited *in vivo* (zebrafish embryos and adult mice) by the TGL inhibitor XEN445.[46] Therefore, we investigated the influence of XEN445 on the lipolytic activity of LPL on PAP3. LPL was incubated with XEN445 at room temperature for 30 min, prior to the addition of LPL to PAP3 liposomes, and DOaG hydrolysis was found to be inhibited by ~50% at 500uM XEN445 (**Figure 3f** and **Figure S9**).

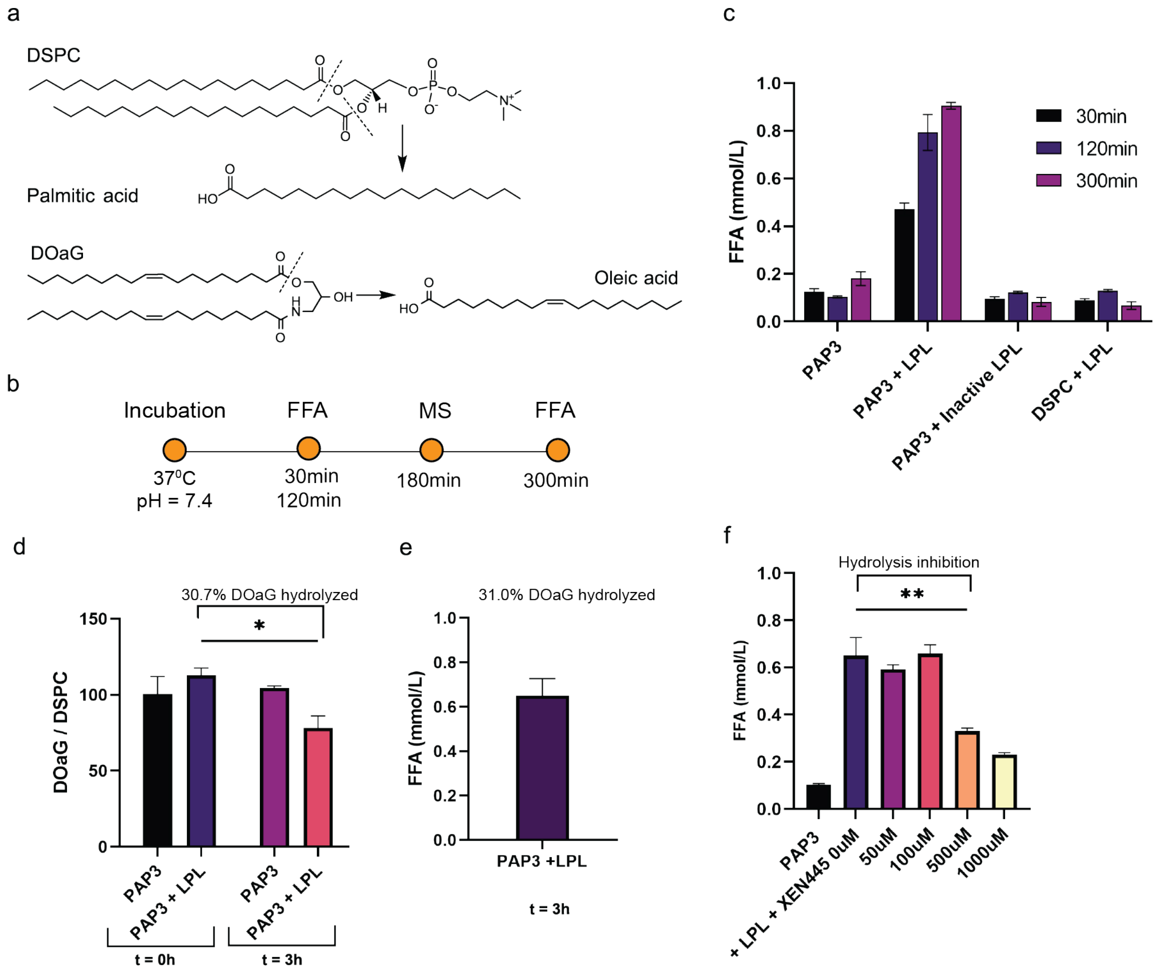

Figure 3. **Hydrolysis of lipids in PAP3 liposomes. a)** Potential hydrolysis of DSPC and/or DOaG co-formulants by LPL resulting in free fatty acid (FFA) release *i.e.*, palmitic or oleic acid, respectively. **b)** Timeline of measurement of LPL hydrolytic activity. Incubation of liposomal formulation at 37 °C, pH = 7.4 and measurement of hydrolysis via quantification of released FFA (after 30,120 and 300 min) or mass spectrometry (after 180 min). **c)** Quantification of released FFA after incubation of PAP3 liposomes without and with LPL, or PAP3 with inactive LPL, or DSPC liposomes with LPL after 30, 120, and 300 min. **d)** Quantification of DOaG / DSPC lipid ratio in PAP3 liposomes as measured by mass spectrometry at t=0 and t=3h incubating at 37 °C with and without LPL. DOaG / DSPC ratio of PAP3 at t=0h was set as 100. Analysis indicated the % of DOaG hydrolyzed. **e)** Quantification of released FFA in PAP3 liposomes incubating with LPL at 37°C for 3h, indicating the % of DOaG hydrolyzed. FFA release was measured immediately after the mass spectrometry analysis. The difference on the released FFA of PAP3 between Figure 3c and 3e is attributed to the different concentrations of LPL used for each measurement and therefore hydrolysis must be designated as a range (0.6-0.9 mmoL/L). **f)** XEN445 mediated inhibition of LPL and effect on FFA release after PAP3 liposomes incubated with LPL and 0, 50, 100, 500 or 1000uM XEN445. Statistical significance was

evaluated using a two-tailed unpaired Student's t-test. ns: not significant ($P > 0.05$). Significantly different: *$P \leq 0.05$, **$P \leq 0.01$, ***$P < 0.001$. Exact P value for d : 0.0337 and for f : 0.0020.

Simulations confirm lipase binds on PAP3 liposomes through lipid packing defects and via its Trp-rich lipoprotein binding domain

Having confirmed that LPL selectively hydrolyzes liposomes containing DOaG, we sought to investigate the role of the characteristic phase-separated morphology. Previously, we showed that the concentration of DOaG lipid in the PAP3 formulation determines whether liposomes phase separate. When PAP3 was formulated with DSPC and 0, 10, or 20 % mol DOaG, liposomes did not show phase separation, while above 30 % mol DOaG liposomes were found phase separated, causing a directed *in vivo* biodistribution towards TGL rich endothelial cells.[13] Therefore, we hypothesized phase separation to be essential, or at least preferable, for TGL recognition. To assess this hypothesis, released FFA after LPL incubation was measured for liposomes with varying % mol of DOaG. Up to 20 % mol, i.e. for mixed membranes, FFA release increased linearly (**Figure 4a, solid line**), but it steeply increased after this point (**Figure 4a, dashed line**). This suggested enhanced LPL action for PAP3 liposomes with ≥30 % mol DOaG, which coincides with the concentration threshold relating to phase separation as quantified by Cryo-TEM (**Figure 4a insets, Figure 4b right y-axis** and **Figure S10**). The finding that the phase change coincides with a non-linear jump in the LPL-induced FFA release, signifies the role of phase separation in LPL hydrolysis.

As reported earlier for DAGs, increasing the DOaG content in a PC bilayer across a phase boundary, could substantially increase the membrane curvature in the surroundings of the lipid droplet. Curvature is known to notably increase the lipid packing defect number and area, an effect that has been suggested to promote protein binding.[17,47] Moreover, compared to a mixed membrane, the local concentration of DOaG in the curved membrane around the lipid droplet is also significantly higher. Therefore, to quantify the role of phase separation, curvature and packing defects at a molecular level - that is not directly accessible by experiments or atomistic MD due to long time scales - we generated a coarse-grained (CG) representation for DSPC/DOaG at different DOaG concentrations (**snapshots** in **Figure 4b** and **Figure S11a**). As detailed in the SI (sections **S12-S15**), the CG DOaG lipid representation was adapted from the similar DOG lipid.[48] In agreement with standard practice, we employed the observed phase separation onset at 29 % mol (**Figure 4b, left y-axis**) to match the experimental findings. Phase separation in CGMD was quantified by the (time-averaged) relative fraction of contacts between the DOaG lipid and the DSPC lipid (see Materials and Methods for more details and

Figure S14) following a recently developed method.[49] The DOaG parametrization described here was used for all simulations in the remainder of this study.

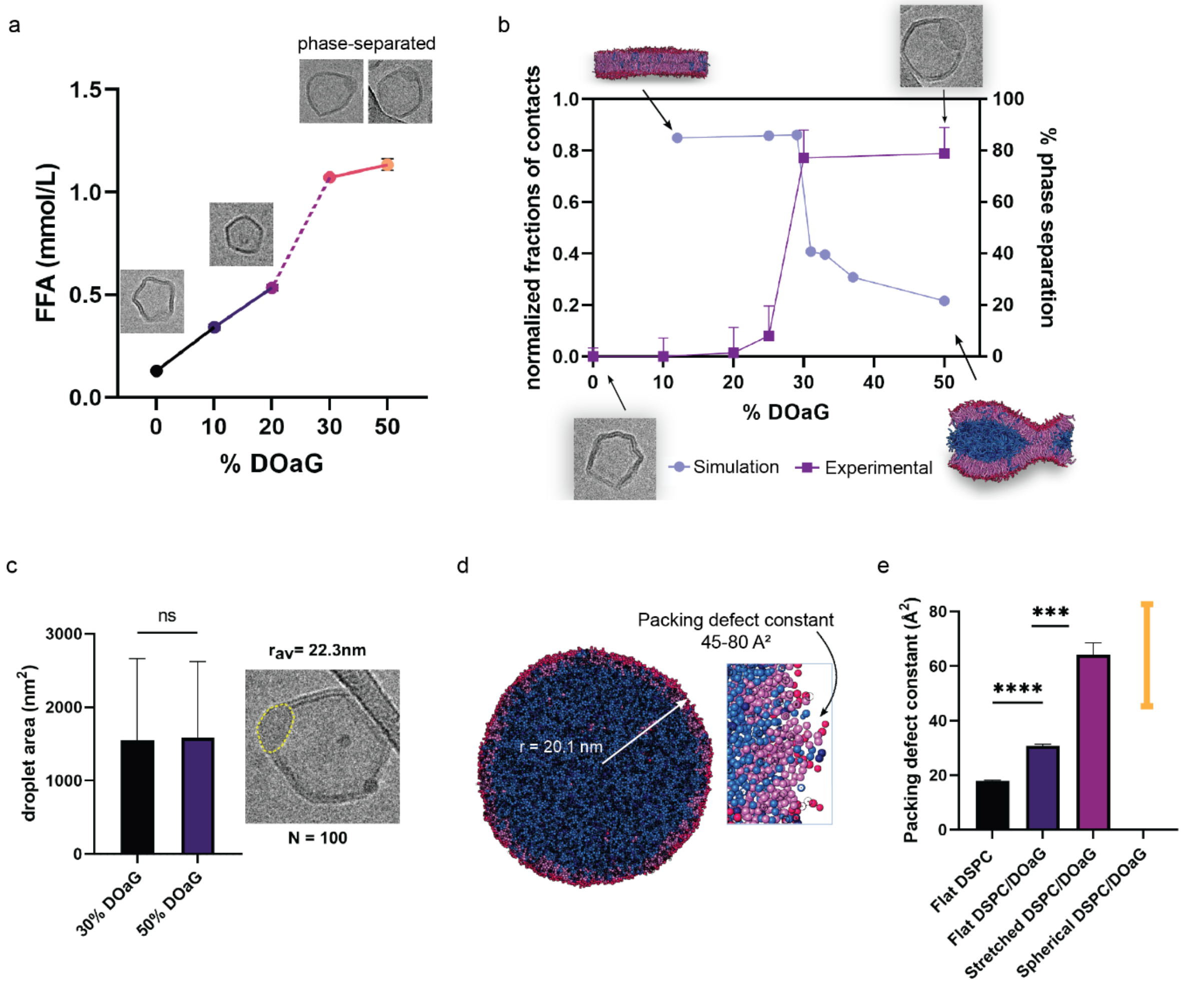

Figure 4. Experimental findings and simulations confirm phase-separation as an important aspect for LPL preferential binding on PAP3 liposomes a) Quantification of released FFA of formulations containing DSPC and varying % mol of DOaG after incubation with LPL for 120 min. Insets show the morphology of liposomes at a particular % mol DOaG (0 % = gel phase, 20 % = small droplet indicate initiation of phase-separation, 30-50% = phase-separated). **b)** Double plot showing correlation of experimental and simulation data. Phase separation starts after 25 %mol DOaG according to cryo-TEM quantification (N=200) and 29 % according to the coarse-grained simulation. DOaG is shown in blue and DSPC is shown in pink/red. **Correlation of simulated PAP3 droplet and experimental values. c)** Average radius of phase separated PAP3 liposomes (containing 30 % or 50 % mol DOaG) as calculated by cryo-TEM quantification of the droplet area (N=100). Area was measured in Fiji software, by drawing the perimetry of each droplet (yellow dashed line) according to the electron density. Experimental values were obtained to correlate the simulation data for the PAP3 model droplet. **d)** Simulated PAP3 droplet with radius approximately matching the experimental value and zoom-in inset depicting the lipid packing defects. Packing defect constant determined as the effective average area of hydrophobic defects and calculated to be 45-80 Å^2 for the spherical droplet. DOaG is shown in blue and DSPC is shown in pink/red. **e)** Packing defect constants of flat DSPC, flat DSPC/DOaG, streched DSPC/DOaG and packing defect constant range (in orange) of spherical DSPC/DOaG (see d). Statistical

significance was evaluated using a two-tailed unpaired Student's t-test. ns: not significant ($P > 0.05$). Significantly different: *$P \leq 0.05$, **$P \leq 0.01$, ***$P < 0.001$. Exact P value for c: 0.8152, e: 0.0002 and <0.0001. For graphs in a and b, lines were drawn for the clear visualization of the phase separation point.

To capture the role of curvature and to quantify the defect characteristics for a DSPC monolayer embedding the DOaG droplet of a typical diameter - i.e. an average of 22.3 nm for ≥30 %mol DOaG (see **Figure 4c**) as quantified by cryo-TEM - we performed a droplet simulation with this initial radius for a 82/18 DOaG/DSPC ratio (**Figure 4d** and **Figure S11b**). Since demixing is strongly diffusion limited, we started from a pre-structured droplet and performed 2 microsecond of simulated annealing, to quickly reach a stable structure, with the droplet radius stabilizing to 20.1 nm. Using a modified protocol (see materials and methods), we calculated the packing defect constant, which is a measure of the effective average area of hydrophobic defects (**Figure 4d, e** and **Figure S16**). For flat DSPC the constant was found to be ~18 A^2 while adding the DOaG to the system increased the constant to ~30 A^2 indicating phase separation increases the packing defects. Also adding curvature– calculating the defect constant on the curved droplet – increases the packing defect constant even further. For the latter, however, we can only give a range since the lipid composition in the droplet monolayer varies, depending on the starting configuration and size, and because there is an uncertainty in the fitting parameter. The range for the packing defect constant found was between 45 to 80 A^2, showing that the packing defects in the curved droplet are more prevalent than in the flat pure DSPC and flat DSPC/DOaG membranes (**Figure 4d zoom in, and Figure 4e**). We next used this value range as a reference value for the simulation of LPL binding to stretched DOaG/DSPC membranes (**Figure 4e and 5c**) as a proxy for curvature[50] (*vide infra*).

Following the proof that the DOaG droplet increases both the number and area of lipid packing defects in the curved DSPC monolayer - due to the condensing of DOaG and the accompanying high curvature of the outer leaflet - we next sought to investigate whether LPL specifically binds to PAP3 via these packing defects. The structure of LPL is well studied and identified by X-ray crystallography[51] and Cryo-TEM[52] (**Figure 5a** and **Figure S15**). Functional parts include the lipoprotein binding domain which is rich in Trp as mentioned previously (hence called the Trp-rich loop, **Figure 5a, inset**) and the catalytic lid with the active site (**Figure 5a, inset**). The C-terminus, where the lipoprotein binding domain is located, is responsible for substrate binding but not for heparin binding or catalysis.[53] We first proceeded to investigate which regions of the LPL protein may be involved in interacting with the lipid packing defects of the phase separated membrane. Hereto, we employed a recently developed neural network (NN) model that is trained on MD data and is able to predict the lipid packing defect sensing free energy (ΔΔF) for peptide sequences.[54] ΔΔF is defined as the difference in free energy of a peptide binding to a tensionless membrane versus a stretched membrane that bares lipid packing defects, such as the curved lipid monolayer around a lipid droplet. The higher the magnitude of the ΔΔF value, the more favorably it binds to the defected membrane. We first used a sliding window of 15 residues to fragmentize the LPL protein structure and then predicted the ΔΔF for the overlapping fragments. From this, we derived a per-residue average ΔΔF (given the residue is solvent accessible, see section **S17** and **Figure S18**) and color-coded the protein structure accordingly (**Figure 5b**).

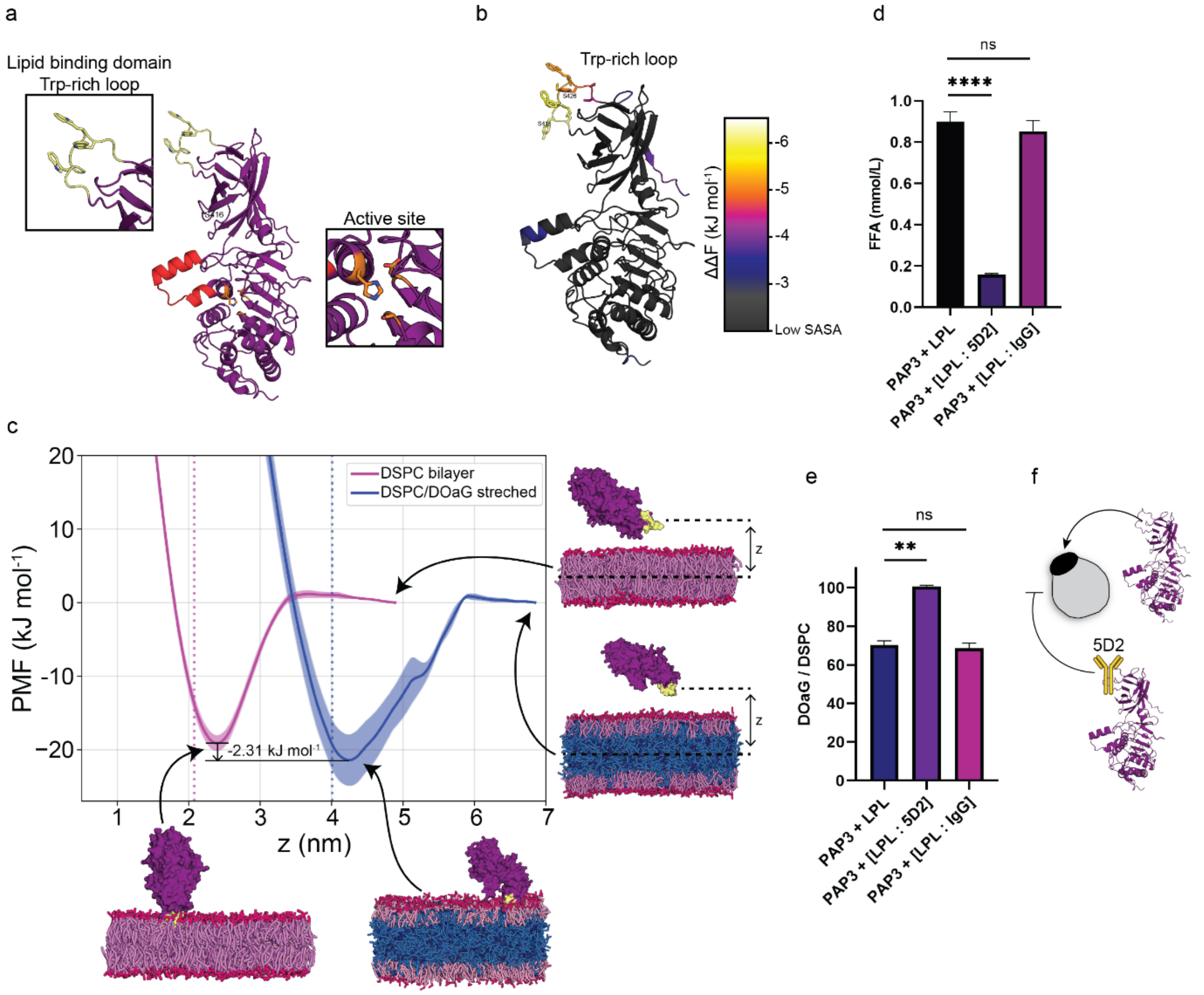

Figure 5. LPL binds to PAP3 liposomes via its Trp-loop. a) Structure of LPL (*Bos Taurus*). Insets indicate the Trp-rich loop (yellow) - which comprises the lipoprotein binding domain - and active site (orange). Lid region indicated in red. **b)** Color-map of predicted lipid packing defect sensing regions on LPL (all values are given in **S19**). Bright colors indicate putative sensing motifs, according to NN-predicted relative binding free energy (ΔΔF) and SASA values. **c)** Potential of mean force (PMF) profiles of LPL binding to a DSPC membrane (in red-pink) and a DSPC/DOaG phase separated membrane (in red-pink/blue). The US reaction coordinate is the z-distance between the center-of-mass (COM) of the Trp-rich loop (in yellow) and the COM of the lipids (*i.e.,* center plane of the membrane).

Snapshots are the final frames of the trajectories and indicate that the protein is completely unbound at high z (free energy = 0 kJ mol^{-1}) and membrane-bound through the Trp-rich loop at the minima. Dotted lines indicate the position of the DSPC head groups (NC3 beads). **d)** Quantification of released FFA from PAP3 liposomes after incubation for 120 min with LPL, LPL + 5D2 antibody and LPL + IgG control antibody. **e)** Mass spectrometry quantification of DOaG / DSPC ratio of PAP3 liposomes incubating for 120 min with LPL, LPL+ 5D2 antibody and LPL + IgG control antibody. DOaG/DSPC ratio of liposomes that did not undergo hydrolysis incubating with LPL + 5D2 was set as 100. **f)** Schematic of LPL binding to PAP3 liposomes via its Trp-rich loop and 5D2 mediated inhibition of binding. Statistical significance was evaluated using a two-tailed unpaired Student's t-test. ns: not significant ($P > 0.05$). Significantly different: $*P \leq 0.05$, $**P \leq 0.01$, $***P < 0.001$. Exact P value for d : <0.0001 and 0.3222 and for e : 0.0029 and 0.5654.

Residues Ser416-Ser426, comprising the Trp-rich loop, was the highest scoring solvent-accessible peptide motif we identified (**Figure 5b** and section **S19**). As previously described in the context of membrane curvature sensing, Trp residues can indeed play a key role in complementing the hydrophobic lipid packing defects on lipid leaflets,[25] and we argue that the Trp-rich loop of LPL might fulfill a similar function. Notably, this argument is in line with the Trp-rich loop being part of the lipoprotein binding domain of LPL, which is responsible for endogenous lipoprotein binding. [38–40]

To further investigate lipid packing defect sensing by LPL and to see whether the Trp-loop is preferably binding to defected membranes such as the PAP3 liposomes, we calculated the potential of mean force (PMF) profiles for the entire LPL protein binding to the PAP3 phase separated membrane - with lipid packing defect constants that are in the same range as those for the earlier considered PAP3 droplet (*vide supra*, **Figure 4e**). We performed umbrella sampling (US) simulations with the z-distance between the Trp-rich loop and the center plane of the membrane as the reaction coordinate. The resulting potential of mean force (PMF) profiles showed LPL binding to the PAP3 phase-separated membrane (having enhanced lipid packing defects) is indeed more favorable than binding to a flat pure DSPC bilayer, with a small free energy difference of 2.31 kJ mol^{-1} (~1 k_BT) between the minima (**Figure 5c**). The propensity for binding that is observed for the flat pure DSPC membrane (about 20 kJ mol^{-1}) corresponds exactly to the curvature sensing transition point from a recent study[54], which showed that a 2 kJ mol^{-1} increase in binding free energy has a pronounced effect on the membrane binding probability. Moreover, although a conformational change in the binding domain may contribute a few kJ mol^{-1} to the actual binding affinity[55], this shift is likely very similar for both membranes. Beyond this binding preference, the enzymatic preference of LPL to hydrolyze DAGs over phospholipids[56] *is not* captured by our MD simulations but *does* contribute to our experimental observations. From the MD trajectories, it is clear that LPL indeed interacts with the membranes through its Trp-rich loop (**snapshots** in **Figure 5c**), in line with the NN-predictions (**Figure 5b**), and mechanistically similar to previously reported lipid droplet sensing proteins.[57,58]

To experimentally assess the involvement of the Trp-rich loop in the recognition and hydrolysis of PAP3 liposomes, we measured the hydrolytic activity of LPL on PAP3 liposomes, while blocking the Trp-rich loop with the monoclonal anti-LPL antibody 5D2. The 5D2 monoclonal antibody has been identified to bind specifically to the Trp-loop of the lipid binding domain of LPL, inhibiting binding and catalysis of lipoproteins.[40,59–61] Indeed, after incubation of LPL with 5D2 in a 1:1 ratio at room temperature for 30 min and subsequent addition to PAP3 liposomes, hydrolysis of DOaG as quantified by the release of FFA and mass spectrometry was strongly reduced (**Figure 5d-f**). To ensure that inhibition of hydrolysis was due to the specific inhibition of the Trp-rich loop by the 5D2 antibody, a negative isotype control antibody (matching 5D2 antibody's host species and class - IgG1) was used to measure the non-specific binding in LPL and non-specific interactions with PAP3. As expected, the control antibody did not inhibit the hydrolysis (**Figure 5d, e**), supporting the specific interaction of LPL with PAP3 liposomes through its Trp-rich loop. Similarly, when a non-mammalian LPL (derived from *Burkholderia sp.*) - which lacks the conserved lipoprotein binding domain of mammalian TGLs - was used with the 5D2 antibody (**Figure S20** for complete sequence), hydrolysis was not inhibited (**Figure S21**), indicating again the specificity of 5D2 to the Trp-rich loop. Despite the hydrolysis of PAP3 liposomes taking place with the non-mammalian lipase, it appears to occur via a different mechanism, and it is therefore not relevant for the study of mammalian LPL species. It *does* however signify that 5D2 inhibits the Trp-loop specifically, and non-specific interactions between antibody-protein-liposomes do not take place.

DISCUSSION

In this work, we combine experimental findings and MD simulation data to describe the selective lipolytic degradation of lipid droplets in phase-separated liposomes by LPL. We show LPL recognizes the enhanced lipid packing defects on the liposomal membrane induced by phase separation. The liposomes, named PAP3, consist of the naturally occurring DPSC and the synthetic DAG analogue DOaG, which is responsible for the phase separation and constitution of a lipid droplet within each liposome bilayer. PAP3 liposomes have been seen to specifically interact with TGLs *in vivo*[13], a phenomenon attributed to their phase separated morphology. Therefore, the observation of their structural evolution after interaction with LPL, as well as the mechanism of enzyme binding was of great interest. Here, we confirm the selective hydrolysis of DOaG by LPL, leading to degradation of the DOaG droplet and to reorganization of the assembly to a lamellar bilayer, while the overall integrity of the nanoparticle is maintained. Contrarily, the other co-formulant – DSPC – does not undergo hydrolysis. These observations exemplify selective nanoparticle-protein interactions and subsequent nanoparticle rearrangement. As TGLs endogenously remodel lipoproteins without nanoparticle collapse – *i.e.,* LPL remodels very low-density lipoproteins to low-density lipoproteins[34,62,63] - here we similarly show the depletion of a large part of the nanoparticle without bilayer disruption.

Additionally, we show that LPL is selective for PAP3 liposomes (DSPC/DOaG) and for liposomes containing the natural DAG counterpart (DSPC/DOG). LPL does not hydrolyze 100% DSPC liposomes, or typical spherical LUVs with high circulation lifetimes *in vivo* (*i.e.,* Myocet®-like, POPC/CHO). One reason for this could be the inherent preference of LPL to hydrolyze DAGs and therefore DAG analogues such as DOaG. Synergistically, another reason could be the preference of LPL to recognize membranes with high curvature - and thus higher packing defect constants - induced by phase separation.[15,16,24] This hypothesis is supported by the non-linear, increased hydrolysis on liposomes consisting of ≥ 30 % DOaG (phase separated) over liposomes consisting of < 25 %mol DOaG (non-phase separated). Lipid packing defects were then quantified in our coarse-grained MD simulations and found to be higher when phase separation and high curvature are present in the membrane system. Finally, we show that LPL preferentially binds to the defected membrane of PAP3 liposomes and we identified the Trp-rich loop of LPL as a lipid packing defect sensing motif. Preventing the Trp-loop to bind to PAP3 (by blocking the region with the selective antibody 5D2 [59]), abolishes the lipolysis and confirms the involvement of the Trp-rich loop in the recognition of PAP3 liposomes. Hereby, we expand our knowledge of the Trp-rich loop to act as a lipid packing defect sensor, beyond its role in lipoprotein binding.[38] PAP3 liposomes appear to hijack the natural pathway in which LPL recognizes lipoproteins via its Trp-rich loop, by their exposed lipid packing defects that arise upon phase separation.

Additionally, we have previously shown that PAP3 liposomes are endocytosed by a TGL-mediated pathway *in vivo*.[13] A possible pathway for this could be the selective recognition of DOaG by TGL - with a significantly higher chance of DOaG being transiently exposed to the aqueous environment due to the increased packing defects in the phase separated membrane -

and subsequent endocytosis. Our current study shows the selective lipolysis and remodeling of the particle by LPL, something that may also occur *in vivo* before nanoparticle uptake by the cell. However, given the complex *in vivo* environment and the spatiotemporal regulation of lipase function in lipid metabolism, further studies should be performed *in vivo* and in real time to solidly prove this.

Another noteworthy observation are the visible remnants of the hydrolyzed droplet on some nanoparticles (**Figure S22, arrows**). Such thickness mismatches in Cryo-TEM have been recently described as nanodomains in liposomal membranes.[64,65] Therefore, although liposomes can be seen as lamellar and non-phase separated macromolecularly, a more in-depth investigation of the molecular details, e.g. the existence of nanodomains or lipid rafts remaining after LPL hydrolysis, is required. The question that arises here is whether such nanodomains can be still recognizable by TGLs *in vivo*.

Finally, the selection of LPL as a representative TGL was purely due to the extensive literature on LPL structure, regulation and function in health and disease, and therefore was the most relevant protein to base our studies on. However, all (mammalian) lipases from the TGL family have very similar amino acid sequences ([36] and **Figure S23** for protein alignment), structural homology, and similar functional roles on triglyceride metabolism.[33,66–68] This allows the assumption that other TGLs will behave similarly on PAP3 liposomes as the LPL studied here. On the same note, the LPL chosen for these studies was derived from bovine milk (*Bos Taurus*), yet the sequence homology with human LPL (*Homo Sapiens*) is > 90 %, with high structural similarity and a conserved Trp-loop (see **Figure S24-S25** for protein structure alignment), which allows to assume that it will similarly affect PAP3 liposomes as bovine LPL. To support this, we show that incubating PAP3 liposomes with human LPL releases a substantial amount of FFA (**Figure S26**). Also, similar PMF profiles were calculated for human LPL interacting with the DOaG/DSPC phase separated membrane and a flat DSPC bilayer through its Trp-rich loop, showing even a more substantial binding preference for the phase-separated system in terms of the free energy difference between the minima (13.48 kJ mol^{-1}) (**Figure S27**).

Overall, this study explains in detail the how and the why of the preferential interaction of TGLs with unique phase separated liposomes induced by DAGs and DAG analogues, an interaction which is responsible for cell specific targeting *in vivo*. It emphasizes the importance of understanding the nanoparticle / protein interface, an aspect that determines the *in vivo* behavior and fate of nanoparticles and if exploited further, it could lead to more precise nanomedicines in the future.

MATERIALS AND METHODS

Liposome formulation

Large unilamellar vesicles (LUVs) were formed through extrusion (mini extruder, Avanti Polar Lipids) above the T_m of all lipids (*i.e.* 65-70 ºC) in 10mM Tris Buffer pH = 7.4 and at a total lipid concentration of 5 mM (3.5 mg/mL), unless if stated otherwise. Individual lipids as stock solutions (10 mM) in chloroform, were combined to the desired molar ratios and dried to a thin film, first under N_2 stream, then >1 h under vacuum. Lipid films were hydrated with 1mL Tris Buffer above the T_m of all lipids (65-70 ºC), with gentle vortexing, to form a suspension. Hydrated lipids were passed 11 times through 2 x 400 nm polycarbonate (PC) membranes (Nucleopore Track-Etch membranes, Whatman), followed by 11 times through 2 x 100 nm PC membranes. All liposomes were stored at 4 ºC and used within 5 days.

Liposome - Lipase Incubation

Liposomes (3.5 mg/mL, in 10mM Tris Buffer, pH = 7.4) were transferred in a low protein binding tube (3 mg/mL final lipid concentration after lipase incubation) and subsequently Lipoprotein Lipase (in 10mM Tris Buffer pH = 7.4) was added to the tube to reach 0.03 mg/mL final concentration. Liposomes – lipase mixture was left to incubate at 37 ºC in a thermomixer for up to 20 h with gentle occasional mixing.

FFA release measurement

For each time point of interest, the amount of FFA resealed in the sample was measured with a non-esterified fatty acid assay kit (NEFA kit – Fujifilm Wako Chemicals) with a protocol provided for 96 well plates (Greiner) using a microplate spectrophotometer set to 37 ºC (Infinite®, M1000 pro, TECAN). Briefly and for each sample, 9 uL were taken and diluted 2x in Tris Buffer 10 mM (pH = 7.4). 5 µL were then put in each well and mixed with 200 µL of Reagent 1 and incubated for 5 min. The absorbance (Abs1) was then measured in each well at 550 nm (Sub: 660 nm). Immediately after, 100 µL of Reagent 2 was added and the mixture was incubated for another 5 min. The absorbance (Abs2) was again then measured in each well at 550 nm (Sub: 660 nm). Final absorbance was calculated by subtracting Abs1 from Abs2. Concentration of FFA (mmoL/L) was calculated by constructing each time a new calibration curve. All measurements were the average of three measurements.

Cryogenic Transmission Electron Microscopy

Freshly glow-discharged carbon grids supported on Cu (Lacey carbon film, 200 mesh, Electron Microscopy Sciences, Aurion, The Netherlands) were used for vitrification inside a Vitrobot plunge-freezer (FEI VitrobotTM Mark III, Thermo Fisher Scientific) regulating steady temperature and humidity conditions (22 ºC or 37 ºC and 99 % humidity). Liposomes incubating with LPL at 37 ºC were immediately taken and applied to the grid and the excess liquid was blotted for 3 s and subsequently plunge frozen in liquid ethane below -160 ºC to ensure formation of vitreous ice. Cryo-EM images were collected on a Talos L120C (NeCEN, Leiden University) operating at 120 kV or on a Titan Krios (TU Eindhoven) operating at 300 kV, with working temperature below -180 ºC. Images were recorded manually at a nominal magnification of 13500x, 22000x or 36000x yielding a pixel size at the specimen of 7.41, 4.44, or 2.86 ångström (Å), respectively.

Simulation details

All simulations were performed with GROMACS 2019.3 [70] and the Martini 3.0.0 force field[48], at a 20-fs time step. Temperature ($T = 303.15$ K, $\tau_T = 1$ ns) and pressure coupling (compressibility = $4.5 \cdot 10^{-5}$ bar^{-1}, $\tau_p = 12$ ns) were applied by the velocity rescaling thermostat and the Berendsen barostat, respectively. The neighbor list was updated every 20 steps. A 1.1 nm cutoff was used for the Van der Waals interactions (shifted Verlet cutoff scheme) and Coulomb interactions (reaction-field electrostatics).

Coarse-grained model for PAP3 liposomes

Phase separation on PAP3 liposomes was determined from the MD trajectories, using the time-averaged contact fraction between the DOaG and the DSPC lipid. Following a general procedure[49], a relative contact fraction was calculated by counting contacts between DOaG and DSPC lipids and dividing it by the total number of DOaG contacts (see sections **S12-S15** for details). A cutoff of 1.1 nm was used to identify contacts between lipids via selected beads on both lipid types that are roughly at the same depth within the membrane. In addition, we normalized by the total concentration of DOaG to enable direct comparison for different DOaG concentrations. Consequently, complete phase separation always corresponds to a value of zero, and ideal mixing to unity.

Droplet simulation

For the simulation of the droplet, the droplet configuration was made with PackMol[71] with - on the inside - purely DOaG and on the outside a monolayer of DSPC. The simulated annealing was run for 1.5µs, with a starting temperature of 450 K and cooled to a temperature of 303 K, after which the temperature was kept stable for 500 ns at the final temperature. After the simulated annealing the droplet was ran for analysis for 1.5 μs at the same temperature and settings as the bilayer simulations.

Packing defects on spherical systems

While previous work used the PackMem package[72] to identify a linearly increasing defect size constant with total curvature for both single component and mixed membranes [19], the role of (de)mixing remains less quantified. Here, we developed a new computational protocol to clarify this relation for our highly curved DOaG/DSPC membranes of arbitrary (non-symmetric) shapes. Packing defect constants for the simulated PAP3 droplet can in principle be determined using standard PackMem routines, by employing a spherical instead of the usual rectangular grid.[19] However, since droplets do not necessarily adopt a purely spherical shape, even tiny mismatches in the determination of the relevant reference interface may bias the calculated constants in a non-predictable fashion. For this reason, we developed a protocol that can deal with arbitrary shapes. Briefly, a closed 2D interface is fitted through the positions of relevant GL beads, subsequently triangulated, and used as a reference for identifying shallow and deep defects following the recommended PackMem settings.[72] Details and examples of this procedure will be published in a separate study.

Protein modeling and lipid packing defect sensing prediction

The 3D models of human and bovine LPL were downloaded from the AlphaFold2 database.[73,74] Both structures closely overlap with the human crystal structure[51] (**Figure S25**). The unstructured N-terminal signal sequence (residue 1-34) was excluded. To predict which regions of the protein may play a role in lipid packing defect sensing, a previously developed neural network model was applied. [54] A sliding window of 15 residues was used to predict binding free energy values ($\Delta\Delta F$) for peptide motifs along the sequence of the bovine LPL protein (section **SI7-S19**). In order to exclude buried protein regions (that are unavailable to interact with membranes), only peptide motifs with an average solvent-accessible surface area (SASA, as calculated using BioPython[75]) of greater than 0.8 nm^2 were considered. To visualize putative regions of interest, the B-factor field in the PDB file format was used to adjust the coloring accordingly.

Umbrella sampling

A DSPC bilayer (361 molecules per leaflet) was prepared using the *insane* python script[76] and the Martini 3 CG force field.[48] After solvation with Martini 3 water and ions (0.15 M NaCl), steepest decent energy minimization and 10 ns of semiisotropic NpT equilibration (p_{ref} = 1 bar) were performed. Next, a layer of 1444 randomly oriented DOaG molecules was inserted between the two DSPC leaflets. The resulting 1:2 DSPC:DOaG trilayer was energy minimized and equilibrated. A 75 bar·nm surface tension was applied to the trilayer system to match the lipid packing defects (measured by PackMem with the recommended settings[72]) to the ones found on a DSPC/DOaG spherical lipid droplet (see **Figure S16**). A CG Martini representation of the LPL protein was obtained with Martinize2/VerMOUTH.[77] Secondary structure was predicted with DSSP[78] and constrained by an elastic network between the backbone beads (k_{force} = 500 kJ mol^{-1}). The CG protein was inserted into the bilayer/trilayer systems with ~4 nm separation between the Trp-rich loop of the protein (Ile413-Pro427) and the upper leaflet's lipid head groups. The resulting set-ups were resolvated with water and ions (0.15 M NaCl). After steepest decent energy minimization, both systems were equilibrated for 100 ns with position restraints (k_{force} = 1,000 kJ mol^{-1}) on all protein beads. The initial frames for umbrella sampling (US) were generated by running a pulling simulation in which the z-distance between the centers-of-mass (COM) of the Trp-rich loop and the lipids was decreased gradually, and then selecting 24 frames that span the range from the solvated to the membrane-bound state with 0.2 nm increments. For each umbrella window, a 50 ns equilibration followed by a 2 µs production run was performed in which the Lipid-Trp-rich loop COM z-distance was constrained to its initial value (k_{force} = 500 kJ mol^{-1}). To dampen membrane deformations during US runs, a soft harmonic flat-bottom potential (k_{force} = 100 kJ mol^{-1}) was applied on the lipid head groups to restrain the lipids within its initial thickness range (+0.5 nm on each side of the membrane). Free energy profiles were obtained through umbrella integration[79] with 10,000 bins. Averages and standard deviations were calculated by using block-averaging over 3 blocks.

ACKNOWLEDGMENTS

This work was supported by the Netherlands Organization for Scientific Research (NWO-VICI – project nr. 724.014.001 awarded to A.K.) and by a Leiden/Huygens Scholarship grant supporting P.P. This work was also supported by the Deutsche Forschungsgemeinschaft (DFG, German Research Foundation) under Germany's Excellence Strategy - EXC 2033 - 390677874 - RESOLV. We also thank the NWO Vidi scheme (project number 723.016.005), and the DFG (grant number RI2791/2-1) for funding H.J.R and N.v.H. This work was also benefited from access to the Netherlands Centre for Electron Nanoscopy (NeCEN) at Leiden University, an Instruct-ERIC center, with technical assistance from Ludovic Renault, Willem Noteborn and Birgit Luef. The Dutch Research Organization NWO (Snellius@Surfsara) and the HLRN Göttingen/Berlin are acknowledged for the provided computational resources. We would like to thank Fred Campbell, Roy Pattipeiluhu and Aleksandra Chikunova for fruitful discussions that helped realizing this project.

REFERENCES

(1) Bulbake, U.; Doppalapudi, S.; Kommineni, N.; Khan, W. Liposomal Formulations in Clinical Use: An Updated Review. *Pharmaceutics* **2017**, *9* (2), 12.

(2) Cullis, P. R.; Hope, M. J. Lipid Nanoparticle Systems for Enabling Gene Therapies. *Molecular Therapy* **2017**, *25* (7), 1467–1475.

(3) Akinc, A.; Maier, M. A.; Manoharan, M.; Fitzgerald, K.; Jayaraman, M.; Barros, S.; Ansell, S.; Du, X.; Hope, M. J.; Madden, T. D.; Mui, B. L.; Semple, S. C.; Tam, Y. K.; Ciufolini, M.; Witzigmann, D.; Kulkarni, J. A.; van der Meel, R.; Cullis, P. R. The Onpattro Story and the Clinical Translation of Nanomedicines Containing Nucleic Acid-Based Drugs. *Nature Nanotechnology* **2019**, *14* (12), 1084–1087.

(4) Kulkarni, J. A.; Darjuan, M. M.; Mercer, J. E.; Chen, S.; van der Meel, R.; Thewalt, J. L.; Yi Tam, Y. C.; Cullis, P. R. On the Formation and Morphology of Lipid Nanoparticles Containing Ionizable Cationic Lipids and SiRNA. *ACS Nano* **2018**, *12* (5), 4787–4795.

(5) Schoenmaker, L.; Witzigmann, D.; Kulkarni, J. A.; Verbeke, R.; Kersten, G.; Jiskoot, W.; Crommelin, D. J. A. mRNA-Lipid Nanoparticle COVID-19 Vaccines: Structure and Stability. *Int J Pharm* **2021**, *601*, 120586.

(6) Hou, X.; Zaks, T.; Langer, R.; Dong, Y. Lipid Nanoparticles for mRNA Delivery. *Nature Reviews Materials* **2021**, *6* (12), 1078–1094.

(7) Francia, V.; Schiffelers, R. M.; Cullis, P. R.; Witzigmann, D. The Biomolecular Corona of Lipid Nanoparticles for Gene Therapy. *Bioconjug Chem* **2020**, *31* (9), 2046–2059.

(8) Pattipeiluhu, R.; Crielaard, S.; Klein-Schiphorst, I.; Florea, B. I.; Kros, A.; Campbell, F. Unbiased Identification of the Liposome Protein Corona Using Photoaffinity-Based Chemoproteomics. *ACS Cent Sci* **2020**, *6* (4), 535–545.

(9) Hadjidemetriou, M.; McAdam, S.; Garner, G.; Thackeray, C.; Knight, D.; Smith, D.; Al-Ahmady, Z.; Mazza, M.; Rogan, J.; Clamp, A.; Kostarelos, K. The Human In Vivo Biomolecule Corona onto PEGylated Liposomes: A Proof-of-Concept Clinical Study. *Advanced Materials* **2019**, *31* (4), 1803335.

(10) Hadjidemetriou, M.; Kostarelos, K. Evolution of the Nanoparticle Corona. *Nature Nanotechnology* **2017**, *12* (4), 288–290.

(11) Holme, M. N.; Rashid, M. H.; Thomas, M. R.; Barriga, H. M. G.; Herpoldt, K. L.; Heenan, R. K.; Dreiss, C. A.; Bañuelos, J. L.; Xie, H. N.; Yarovsky, I.; Stevens, M. M. Fate of Liposomes in the Presence of Phospholipase C and D: From Atomic to Supramolecular Lipid Arrangement. *ACS Cent Sci* **2018**, *4* (8), 1023–1030.

(12) Fong, W. K.; Sánchez-Ferrer, A.; Rappolt, M.; Boyd, B. J.; Mezzenga, R. Structural Transformation in Vesicles upon Hydrolysis of Phosphatidylethanolamine and Phosphatidylcholine with Phospholipase C. *Langmuir* **2019**, *35* (46), 14949–14958.

(13) Arias-Alpizar, G.; Papadopoulou, P.; Rios, X.; Reddy Pulagam, K.; Moradi, M.-A.; Pattipeiluhu, R.; Bussmann, J.; Sommerdijk, N.; Llop, J.; Kros, A.; Campbell, F. Phase-Separated Liposomes Hijack Endogenous Lipoprotein Transport and Metabolism Pathways to Target Subsets of Endothelial Cells in Vivo. *Adv Healthc Mater* **2023**, 2202709.

(14) Bolen, E. J.; Sando, J. J. Effect of Phospholipid Unsaturation on Protein Kinase C Activation. *Biochemistry* **1992**, *31* (25), 5945–5951.

(15) Goñi, F. M.; Alonso, A. Structure and Functional Properties of Diacylglycerols in Membranes. *Prog Lipid Res* **1999**, *38* (1), 1–48.

(16) Goldberg, E. M.; Lester, D. S.; Borchardt, D. B.; Zidovetzki, R. Effects of Diacylglycerols on Conformation of Phosphatidylcholine Headgroups in Phosphatidylcholine/Phosphatidylserine Bilayers. *Biophys J* **1995**, *69* (3), 965–973.

(17) Campomanes, P.; Zoni, V.; Vanni, S. Local Accumulation of Diacylglycerol Alters Membrane Properties Nonlinearly Due to Its Transbilayer Activity. *Commun Chem* **2019**, *2* (1), 1–8.

(18) Alwarawrah, M.; Hussain, F.; Huang, J. Alteration of Lipid Membrane Structure and Dynamics by Diacylglycerols with Unsaturated Chains. *Biochim Biophys Acta Biomembr* **2016**, *1858* (2), 253–263.

(19) Vanni, S.; Hirose, H.; Barelli, H.; Antonny, B.; Gautier, R. A Sub-Nanometre View of How Membrane Curvature and Composition Modulate Lipid Packing and Protein Recruitment. *Nature Communications* **2014**, *5* (1), 1–10.

(20) Alwarawrah, M.; Dai, J.; Huang, J. Modification of Lipid Bilayer Structure by Diacylglycerol: A Comparative Study of Diacylglycerol and Cholesterol. *J Chem Theory Comput* **2012**, *8* (2), 749–758.

(21) Goldberg, E. M.; Lester, D. S.; Borchardt, D. B.; Zidovetzki, R. Effects of Diacylglycerols and Ca2+ on Structure of Phosphatidylcholine/Phosphatidylserine Bilayers. *Biophys J* **1994**, *66*, 382–393.

(22) Vamparys, L.; Gautier, R.; Vanni, S.; Bennett, W. F. D.; Tieleman, D. P.; Antonny, B.; Etchebest, C.; Fuchs, P. F. J. Conical Lipids in Flat Bilayers Induce Packing Defects Similar to That Induced by Positive Curvature. *Biophys J* **2013**, *104* (3), 585.

(23) Drin, G.; Casella, J.-F.; Gautier, R.; Boehmer, T.; Schwartz, T. U.; Antonny, B. A General Amphipathic A-Helical Motif for Sensing Membrane Curvature. *Nat Struct Mol Biol* **2007**, *14* (2), 138-146.

(24) Hatzakis, N. S.; Bhatia, V. K.; Larsen, J.; Madsen, K. L.; Bolinger, P. Y.; Kunding, A. H.; Castillo, J.; Gether, U.; Hedegård, P.; Stamou, D. How Curved Membranes Recruit Amphipathic Helices and Protein Anchoring Motifs. *Nature Chemical Biology* **2009**, *5* (11), 835–841.

(25) Vanni, S.; Vamparys, L.; Gautier, R.; Drin, G.; Etchebest, C.; Fuchs, P. F. J.; Antonny, B. Amphipathic Lipid Packing Sensor Motifs: Probing Bilayer Defects with Hydrophobic Residues. *Biophys J* **2013**, *104* (3), 575.

(26) Wildermuth, K. D.; Monje-Galvan, V.; Warburton, L. M.; Klauda, J. B. Effect of Membrane Lipid Packing on Stable Binding of the ALPS Peptide. *J Chem Theory Comput* **2019**, *15* (2), 1418–1429.

(27) Kim, S.; Oh, M. I.; Swanson, J. M. J. Stressed Lipid Droplets: How Neutral Lipids Relieve Surface Tension and Membrane Expansion Drives Protein Association. *Journal of Physical Chemistry B* **2021**, *125* (21), 5572–5586.

(28) Barlič, A.; Gutiérrez-Aguirre, I.; Caaveiro, J. M. M.; Cruz, A.; Ruiz-Argüello, M.-B.; Pérez-Gil, J.; González-Mañas, J. M. Lipid Phase Coexistence Favors Membrane

Insertion of Equinatoxin-II, a Pore-Forming Toxin from Actinia Equina. *J Biol Chem* **2004**, *279* (33), 34209–34216.

(29) Ahyayauch, H.; Sot, J.; Collado, M. I.; Huarte, N.; Requejo-Isidro, J.; Alonso, A.; Goñi, F. M. End-Product Diacylglycerol Enhances the Activity of PI-PLC through Changes in Membrane Domain Structure. *Biophys J* **2015**, *108* (7), 1672.

(30) Bohr, S. S. R.; Thorlaksen, C.; Kühnel, R. M.; Günther-Pomorski, T.; Hatzakis, N. S. Label-Free Fluorescence Quantification of Hydrolytic Enzyme Activity on Native Substrates Reveals How Lipase Function Depends on Membrane Curvature. *Langmuir* **2020**, *36* (23), 6473–6481.

(31) Fuki, I. v.; Blanchard, N.; Jin, W.; Marchadier, D. H. L.; Millar, J. S.; Glick, J. M.; Rader, D. J. Endogenously Produced Endothelial Lipase Enhances Binding and Cellular Processing of Plasma Lipoproteins via Heparan Sulfate Proteoglycan-Mediated Pathway. *Journal of Biological Chemistry* **2003**, *278* (36), 34331–34338.

(32) Merkel, M.; Kako, Y.; Radner, H.; Cho, I. S.; Ramasamy, R.; Brunzell, J. D.; Goldberg, I. J.; Breslow, J. L. Catalytically Inactive Lipoprotein Lipase Expression in Muscle of Transgenic Mice Increases Very Low Density Lipoprotein Uptake: Direct Evidence That Lipoprotein Lipase Bridging Occurs in Vivo. *Proc Natl Acad Sci U S A* **1998**, *95* (23), 13841–13846.

(33) Connelly, P. W. The Role of Hepatic Lipase in Lipoprotein Metabolism. *Clinica Chimica Acta* **1999**, *286* (1–2), 243–255.

(34) Mead, J. R.; Irvine, S. A.; Ramji, D. P. Lipoprotein Lipase: Structure, Function, Regulation, and Role in Disease. *Journal of Molecular Medicine* **2002**, *80* (12), 753–769.

(35) Jaye, M.; Lynch, K. J.; Krawiec, J.; Marchadier, D.; Maugeais, C.; Doan, K.; South, V.; Amin, D.; Perrone, M.; Rader, D. J. A Novel Endothelial-Derived Lipase That Modulates HDL Metabolism. *Nature Genetics* **1999**, *21* (4), 424–428.

(36) Wang, Z.; Li, S.; Sun, L.; Fan, J.; Liu, Z. Comparative Analyses of Lipoprotein Lipase, Hepatic Lipase, and Endothelial Lipase, and Their Binding Properties with Known Inhibitors. *PLoS One* **2013**, *8* (8), 72146.

(37) Choi, S. Y.; Hirata, K.; Ishida, T.; Quertermous, T.; Cooper, A. D. Endothelial Lipase. *J Lipid Res* **2002**, *43* (11), 1763–1769.

(38) Lookene, A.; Groot, N. B.; Kastelein, J. J. P.; Olivecrona, G.; Bruin, T. Mutation of Tryptophan Residues in Lipoprotein Lipase. Effects on Stability, Immunoreactivity, and Catalytic Properties. *J Biol Chem* **1997**, *272* (2), 766–772.

(39) Williams, S. E.; Inoue, I.; Tran, H.; Fry, G. L.; Pladet, M. W.; Iverius, P. H.; Lalouel, J. M.; Chappell, D. A.; Strickland, D. K. The Carboxyl-Terminal Domain of Lipoprotein Lipase Binds to the Low Density Lipoprotein Receptor-Related Protein/Alpha 2-Macroglobulin Receptor (LRP) and Mediates Binding of Normal Very Low Density Lipoproteins to LRP. *Journal of Biological Chemistry* **1994**, *269* (12), 8653–8658.

(40) Goulbourne, C. N.; Gin, P.; Tatar, A.; Nobumori, C.; Hoenger, A.; Jiang, H.; Grovenor, C. R. M.; Adeyo, O.; Esko, J. D.; Goldberg, I. J.; Reue, K.; Tontonoz, P.; Bensadoun, A.; Beigneux, A. P.; Young, S. G.; Fong, L. G. The GPIHBP1-LPL Complex Is Responsible for the Margination of Triglyceride-Rich Lipoproteins in Capillaries. *Cell Metab* **2014**, *19* (5), 849–860.

(41) Yu, J. E.; Han, S. Y.; Wolfson, B.; Zhou, Q. The Role of Endothelial Lipase in Lipid Metabolism, Inflammation and Cancer. *Histol Histopathol* **2018**, *33* (1) 1–10.

(42) Borén, J.; Lookene, A.; Makoveichuk, E.; Xiang, S.; Gustafsson, M.; Liu, H.; Talmud, P.; Olivecrona, G. Binding of Low Density Lipoproteins to Lipoprotein Lipase Is Dependent on Lipids but Not on Apolipoprotein B. *Journal of Biological Chemistry* **2001**, *276* (29), 26916–26922.

(43) de Man, F. H. A. F.; de Beer, F.; van der Laarse, A.; Smelt, A. H. M.; Havekes, L. M. Lipolysis of Very Low Density Lipoproteins by Heparan Sulfate Proteoglycan-Bound Lipoprotein Lipase. *J Lipid Res* **1997**, *38* (12), 2465–2472.

(44) Perdomo, G.; Kim, D. H.; Zhang, T.; Qu, S.; Thomas, E. A.; Toledo, F. G. S.; Slusher, S.; Fan, Y.; Kelley, D. E.; Dong, H. H. A Role of Apolipoprotein D in Triglyceride Metabolism. *J Lipid Res* **2010**, *51* (6), 1298–1311.

(45) Batist, G.; Barton, J.; Chaikin, P.; Swenson, C.; Welles, L. Myocet (Liposome-Encapsulated Doxorubicin Citrate): A New Approach in Breast Cancer Therapy. *Expert Opin Pharmacother* **2002**, *3* (12), 1739–1751.

(46) Sun, S.; Dean, R.; Jia, Q.; Zenova, A.; Zhong, J.; Grayson, C.; Xie, C.; Lindgren, A.; Samra, P.; Sojo, L.; van Heek, M.; Lin, L.; Percival, D.; Fu, J. M.; Winther, M. D.; Zhang, Z. Discovery of XEN445: A Potent and Selective Endothelial Lipase Inhibitor Raises Plasma HDL-Cholesterol Concentration in Mice. *Bioorg Med Chem* **2013**, *21* (24), 7724–7734.

(47) Rigoni, M.; Caccin, P.; Gschmeissner, S.; Koster, G.; Postle, A. D.; Rossetto, O.; Schiavo, G.; Montecucco, C. Equivalent Effects of Snake PLA2 Neurotoxins and Lysophospholipid - Fatty Acid Mixtures. *Science* **2005**, *310* (5754), 1678–1680.

(48) Souza, P. C. T.; Alessandri, R.; Barnoud, J.; Thallmair, S.; Faustino, I.; Grünewald, F.; Patmanidis, I.; Abdizadeh, H.; Bruininks, B. M. H.; Wassenaar, T. A.; Kroon, P. C.; Melcr, J.; Nieto, V.; Corradi, V.; Khan, H. M.; Domański, J.; Javanainen, M.; Martinez-Seara, H.; Reuter, N.; Best, R. B.; Vattulainen, I.; Monticelli, L.; Periole, X.; Tieleman, D. P.; de Vries, A. H.; Marrink, S. J. Martini 3: A General Purpose Force Field for Coarse-Grained Molecular Dynamics. *Nature Methods* **2021**, *18* (4), 382–388.

(49) Liu, Y.; de Vries, A. H.; Pezeshkian, W.; Marrink, S. J. Capturing Membrane Phase Separation by Dual Resolution Molecular Dynamics Simulations. *J. Chem. Theory Comput* **2021**, *17*, 5884.

(50) Hilten, N. van; Stroh, K. S.; Risselada, H. J. Efficient Quantification of Lipid Packing Defect Sensing by Amphipathic Peptides: Comparing Martini 2 and 3 with CHARMM36. *J Chem Theory Comput* **2022**, *18* (7), 4503–4514.

(51) Arora, R.; Nimonkar, A. v.; Baird, D.; Wang, C.; Chiu, C. H.; Horton, P. A.; Hanrahan, S.; Cubbon, R.; Weldon, S.; Tschantz, W. R.; Mueller, S.; Brunner, R.; Lehr, P.; Meier, P.; Ottl, J.; Voznesensky, A.; Pandey, P.; Smith, T. M.; Stojanovic, A.; Flyer, A.; Benson, T. E.; Romanowski, M. J.; Trauger, J. W. Structure of Lipoprotein Lipase in Complex with GPIHBP1. *Proc Natl Acad Sci U S A* **2019**, *116* (21), 10360–10365.

(52) Gunn, K. H.; Roberts, B. S.; Wang, F.; Strauss, J. D.; Borgnia, M. J.; Egelman, E. H.; Neher, S. B. The Structure of Helical Lipoprotein Lipase Reveals an Unexpected Twist in Lipase Storage. *Proc Natl Acad Sci U S A* **2020**, *117* (19), 10254–10264.

(53) Wong, H.; Davis, R. C.; Thuren, T.; Goers, J. W.; Nikazy, J.; Waite, M.; Schotz, M. C. Lipoprotein Lipase Domain Function. J Biol Chem. **1994**, *269* (14), 10319–10323.

(54) Hilten, N. van; Methorst, J.; Verwei, N.; Risselada, H. J. Physics-Based Generative Model of Curvature Sensing Peptides; Distinguishing Sensors from Binders. *bioRxiv* **2022**, 2022.09.01.506157.

(55) Cui, H.; Lyman, E.; Voth, G. A. Mechanism of Membrane Curvature Sensing by Amphipathic Helix Containing Proteins. *Biophys J* **2011**, *100* (5), 1271–1279.

(56) Antamarina-Fojo, S.; Dugi, K. A. Structure, function and role of lipoprotein lipase in lipoprotein metabolism. *Cur Op Lipidol*. **1994**, *5* (2), 117-125.

(57) Prévost, C.; Sharp, M. E.; Kory, N.; Lin, Q.; Voth, G. A.; Farese, R. v.; Walther, T. C. Mechanism and Determinants of Amphipathic Helix-Containing Protein Targeting to Lipid Droplets. *Dev Cell* **2018**, *44* (1), 73-86.e4.

(58) Kim, S.; Swanson, J. M. J.; Voth, G. A. Computational Studies of Lipid Droplets. *Journal of Physical Chemistry B* **2022**, *126* (11), 2145–2154.

(59) Luz, J. G.; Beigneux, A. P.; Asamoto, D. A. K.; He, C.; Song, W.; Allan, C. M.; Morales, J.; Tu, Y.; Kwok, A.; Cottle, T.; Meiyappan, M.; Fong, L. G.; Kim, J. E.; Ploug, M.; Young, S. G.; Birrane, G. The Structural Basis for Monoclonal Antibody 5D2 Binding to the Tryptophan-Rich Loop of Lipoprotein Lipase. *J Lipid Res* **2020**, *61* (10), 1347.

(60) Chang, S. F.; Reich, B.; Brunzell, J. D.; Will, H. Detailed Characterization of the Binding Site of the Lipoprotein Lipase-Specific Monoclonal Antibody 5D2. *J Lipid Res* **1998**, *39* (12), 2350–2359.

(61) Kristensen, K. K.; Leth-Espensen, K. Z.; Mertens, H. D. T.; Birrane, G.; Meiyappan, M.; Olivecrona, G.; Jørgensen, T. J. D.; Young, S. G.; Ploug, M. Unfolding of Monomeric Lipoprotein Lipase by ANGPTL4: Insight into the Regulation of Plasma Triglyceride Metabolism. *Proc Natl Acad Sci U S A* **2020**, *117* (8), 4337–4346.

(62) Wu, S. A.; Kersten, S.; Qi, L. Lipoprotein Lipase and Its Regulators: An Unfolding Story. *Trends in Endocrinology & Metabolism* **2021**, *32* (1), 48–61.

(63) Kersten, S. Physiological Regulation of Lipoprotein Lipase. *Biochimica et Biophysica Acta (BBA) - Molecular and Cell Biology of Lipids* **2014**, *1841* (7), 919–933.

(64) Cornell, C. E.; Mileant, A.; Thakkar, N.; Lee, K. K.; Keller, S. L. Direct Imaging of Liquid Domains in Membranes by Cryo-Electron Tomography. *Proc Natl Acad Sci U S A* **2020**, *117* (33), 19713–19719.

(65) Heberle, F. A.; Doktorova, M.; Scott, H. L.; Skinkle, A. D.; Waxham, M. N.; Levental, I. Direct Label-Free Imaging of Nanodomains in Biomimetic and Biological Membranes by Cryogenic Electron Microscopy. *Proc Natl Acad Sci U S A* **2020**, *117* (33), 19943–19952.

(66) Khetarpal, S. A.; Vitali, C.; Levin, M. G.; Klarin, D.; Park, J.; Pampana, A.; Millar, J. S.; Kuwano, T.; Sugasini, D.; Subbaiah, P. v.; Billheimer, J. T.; Natarajan, P.; Rader, D. J. Endothelial Lipase Mediates Efficient Lipolysis of Triglyceride-Rich Lipoproteins. *PLoS Genet* **2021**, *17* (9).

(67) Olivecrona, G.; Olivecrona, T. Triglyceride Lipases and Atherosclerosis. *Curr Opin Lipidol* **2010**, *21* (5), 409–415.

(68) Watt, M. J.; Spriet, L. L. Triacylglycerol Lipases and Metabolic Control: Implications for Health and Disease. *Am J Physiol Endocrinol Metab* **2010**, *299* (2), 162–168.

(69) Bligh, E. G.; Dyer, W. J. A Rapid Method of Total Lipid Extraction and Purification. *Can J Biochem Physiol* **1959**, *37* (8), 911–917.

(70) Abraham, M. J.; Murtola, T.; Schulz, R.; Páll, S.; Smith, J. C.; Hess, B.; Lindahl, E. GROMACS: High Performance Molecular Simulations through Multi-Level Parallelism from Laptops to Supercomputers. *SoftX* **2015**, *1*, 19–25.

(71) Martinez, L.; Andrade, R.; Birgin, E. G.; Martínez, J. M. PACKMOL: A Package for Building Initial Configurations for Molecular Dynamics Simulations. *J Comput Chem* **2009**, *30* (13), 2157–2164.

(72) Gautier, R.; Bacle, A.; Tiberti, M. L.; Fuchs, P. F.; Vanni, S.; Antonny, B. PackMem: A Versatile Tool to Compute and Visualize Interfacial Packing Defects in Lipid Bilayers. *Biophys J* **2018**, *115* (3), 436–444.

(73) Jumper, J.; Evans, R.; Pritzel, A.; Green, T.; Figurnov, M.; Ronneberger, O.; Tunyasuvunakool, K.; Bates, R.; Žídek, A.; Potapenko, A.; Bridgland, A.; Meyer, C.; Kohl, S. A. A.; Ballard, A. J.; Cowie, A.; Romera-Paredes, B.; Nikolov, S.; Jain, R.; Adler, J.; Back, T.; Petersen, S.; Reiman, D.; Clancy, E.; Zielinski, M.; Steinegger, M.; Pacholska, M.; Berghammer, T.; Bodenstein, S.; Silver, D.; Vinyals, O.; Senior, A. W.; Kavukcuoglu, K.; Kohli, P.; Hassabis, D. Highly Accurate Protein Structure Prediction with AlphaFold. *Nature* **2021**, *596* (7873), 583–589.

(74) Varadi, M.; Anyango, S.; Deshpande, M.; Nair, S.; Natassia, C.; Yordanova, G.; Yuan, D.; Stroe, O.; Wood, G.; Laydon, A.; Zídek, A.; Green, T.; Tunyasuvunakool, K.; Petersen, S.; Jumper, J.; Clancy, E.; Green, R.; Vora, A.; Lutfi, M.; Figurnov, M.; Cowie, A.; Hobbs, N.; Kohli, P.; Kleywegt, G.; Birney, E.; Hassabis, D.; Velankar, S. AlphaFold Protein Structure Database: Massively Expanding the Structural Coverage of Protein-Sequence Space with High-Accuracy Models. *Nucleic Acids Res* **2022**, *50* (D1), D439–D444.

(75) Cock, P. J. A.; Antao, T.; Chang, J. T.; Chapman, B. A.; Cox, C. J.; Dalke, A.; Friedberg, I.; Hamelryck, T.; Kauff, F.; Wilczynski, B.; de Hoon, M. J. L. Biopython: Freely Available Python Tools for Computational Molecular Biology and Bioinformatics. *Bioinformatics* **2009**, *25* (11), 1422–1423.

(76) Wassenaar, T. A.; Ingólfsson, H. I.; Böckmann, R. A.; Tieleman, D. P.; Marrink, S. J. Computational Lipidomics with Insane: A Versatile Tool for Generating Custom Membranes for Molecular Simulations. *J Chem Theory Comput* **2015**, *11* (5), 2144–2155.

(77) Cornelis Kroon, P. Aggregate, Automate, Assemble. **2020**.

(78) Kabsch, W.; Sander, C. Dictionary of Protein Secondary Structure: Pattern Recognition of Hydrogen-Bonded and Geometrical Features. *Biopolymers* **1983**, *22* (12), 2577–2637.

(79) Kästner, J.; Thiel, W. Bridging the Gap between Thermodynamic Integration and Umbrella Sampling Provides a Novel Analysis Method: "Umbrella Integration." *J Chem Phys* **2005**, *123* (14), 144104.

SUPPLEMENTARY INFORMATION for

Lipase-mediated selective hydrolysis of lipid droplets in phase separated-liposomes

*Panagiota Papadopoulou[1#], Rianne van der Pol[1#], Niek van Hilten[1#], Mohammad-Amin Moradi[2], Maria J. Ferraz[3], Johannes M.F.G. Aerts[3], H. Jelger Risselada[1,4,5], G.J. Agur Sevink[6], Alexander Kros[1]**

Table of Contents

Supplementary figures

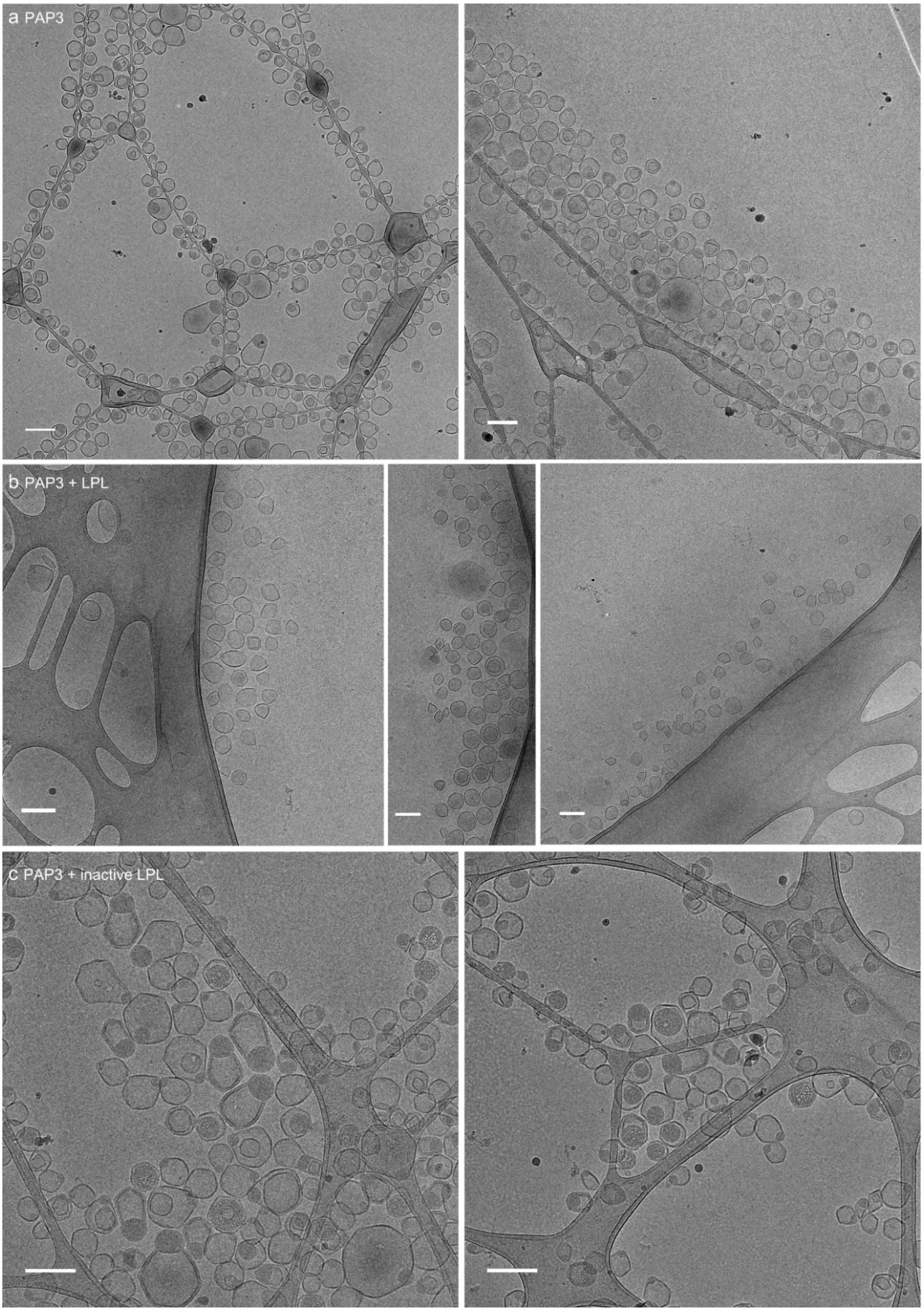

Figure S1. Cryo-TEM images of PAP3 liposomes a) without LPL, **b)** with LPL and **c)** with inactive LPL incubating for 180 min at 37 °C. Images as chosen for quantification of the whole population. Scale bars: 200 nm.

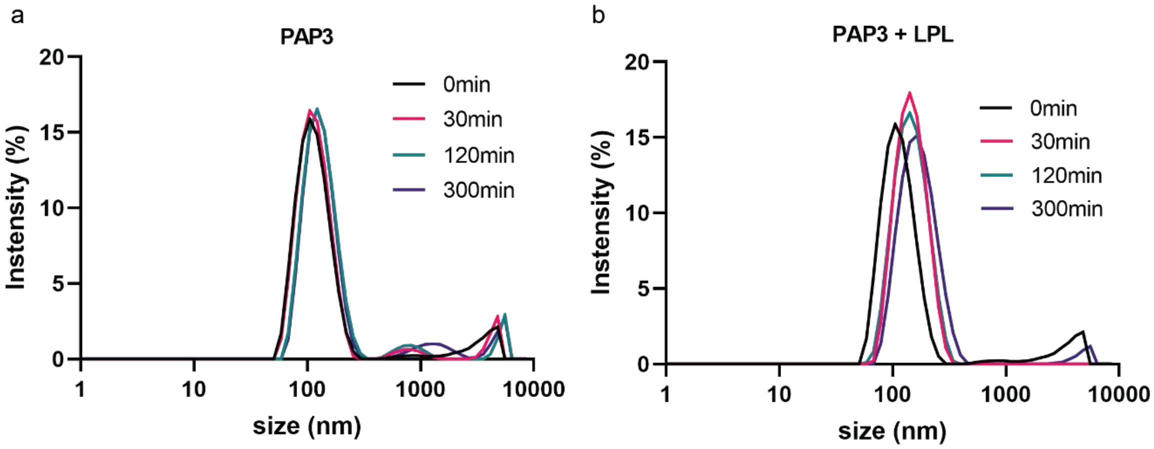

Figure S2. Size of PAP3 liposomes overtime as measured by dynamic light scattering (DLS). a) before and **b)** after addition of LPL. Liposomes incubating at 37 ºC for up to 300 min.

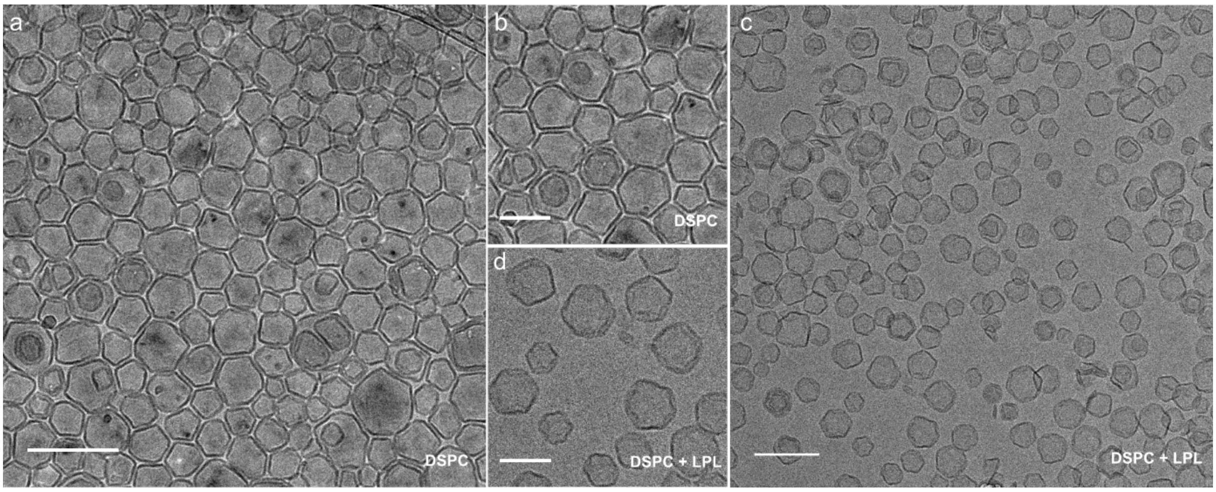

Figure S3. Cryo-TEM images of DSPC liposomes a-b) before and **c-d)** after addition of LPL. Liposomes incubating at 37 ºC for 180 min. Scale bars : 200 nm for a, c and 100 nm for b, d.

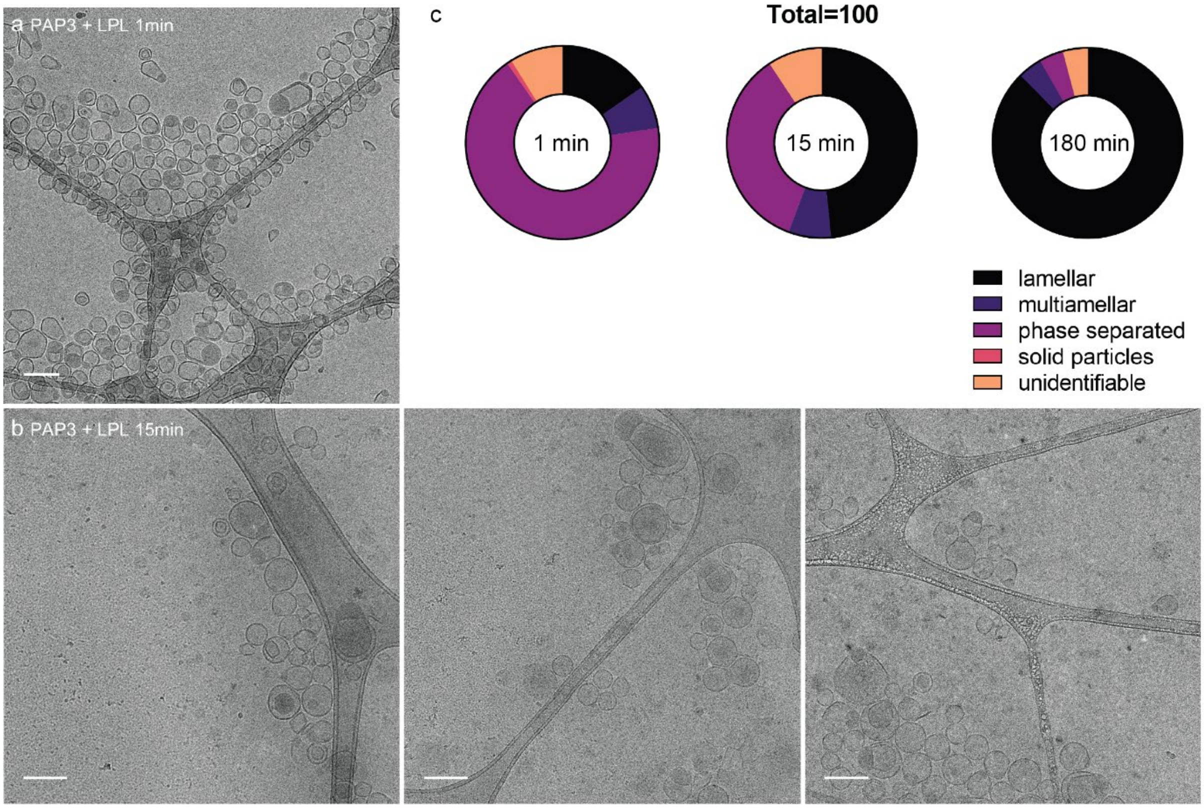

Figure S4. Cryo-TEM images of PAP3 liposomes with LPL incubating at 37ºC for a) 1min or **b)** 15 min and **c)** Quantification of the whole population of PAP3 liposomes with LPL incubating at 37 ºC for 1, 15 and 180 min. Images as chosen for quantification. Scale bars: 200 nm.

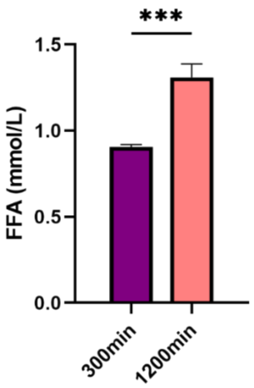

Figure S5. Release of FFA from PAP3 liposomes incubating with LPL. PAP3 liposomes incubating at 37 ºC with LPL for 300 and 1200 min. Statistical significance was evaluated using a two-tailed unpaired Student's t-test. ns: not significant (P > 0.05). Significantly different: *P ≤ 0.05, **P ≤ 0.01; ***P < 0.001. Exact P value 0.0009.

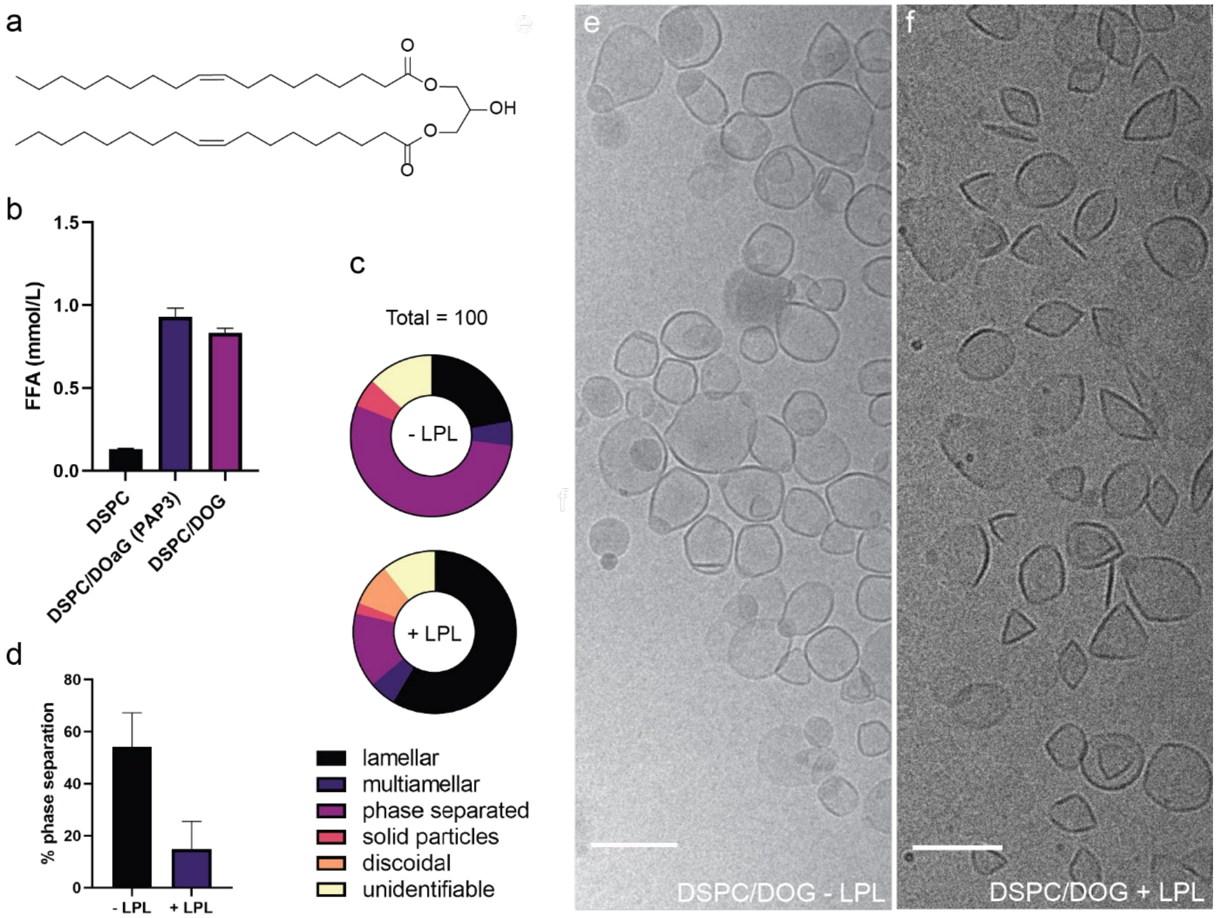

Figure S6. Effect of LPL on DOG containing liposomes. a) Molecular structure of dioleoylglycerol (DOG). **b)** Release of FFA from liposomes containing DSPC (100 %), DSPC/DOaG (50:50), or DSPC/DOG (50:50) after incubation with LPL at 37 ºC for 120 min. **c)** Quantification of the whole population of liposomes consisting of DSPC/DOG (50:50) without LPL or with LPL, incubating at 37 ºC for 120 min. d) Percentage of phase separation of liposomes consisting of DSPC/DOG (50:50) incubating at 37 ºC for 120 min without or with LPL. **e)** Cryo-TEM images of liposomes consisting of DSPC/DOG (50:50) incubating at 37 ºC for 120 min without LPL and **f)** with LPL. Scale bars: 200 nm.

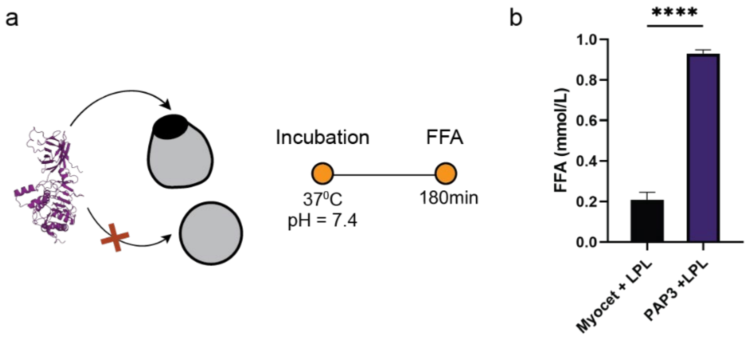

Figure S7. Release of FFA from Myocet®-based formulation in comparison to PAP3 liposomes. a) Schematic of LPL interacting with PAP3 or Myocet®-like liposomes and timeline of measurement of released FFA. **b)** Quantification of released FFA from Myocet®-like or PAP3 liposomes after incubating with LPL at 37 ºC for 180 min. Statistical significance was evaluated using a two-tailed unpaired Student's t-test. ns: not significant (P > 0.05). Significantly different: *P ≤ 0.05, **P ≤ 0.01; ***P < 0.001, ****P < 0.0001. Exact P value : < 0.0001.

			DOaG/DSPC	**% Abundance**
PAP3	.-LPL	t = 0h	0,830483	86,50863
PAP3	.-LPL	t = 0h	0,977713	101,8451
PAP3	.+LPL	t = 0h	1,046577	109,0185
PAP3	.+LPL	t = 0h	0,984694	102,5723
PAP3	.-LPL	t = 3h	0,932472	97,13248
PAP3	.-LPL	t = 3h	0,950282	98,98767
PAP3	.+LPL	t = 3h	0,753585	78,49848
PAP3	.+LPL	t = 3h	0,65356	68,07916

Figure S8. Mass spectrometry analysis of PAP3 liposomes (DOaG:DSPC_50:50). Analysis table of DOaG/DSPC ratio before and after addition of LPL at t = 0 h and t = 3 h (at 37 ºC). Abundance (%) was determined by normalizing all PAP3 data against PAP3 at t = 0 h (average of the two measurements was set as 100 %).

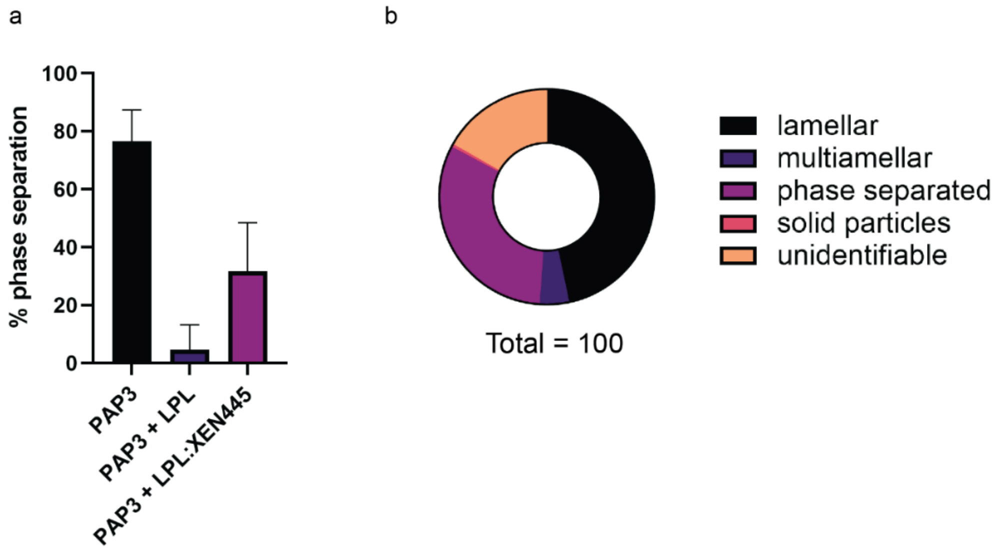

Figure S9. Effect of XEN445 on LPL lipolytic activity. a) Percentage of phase separation of PAP3 liposomes incubating at 37 ºC for 120 min without, or with LPL, or with LPL after addition of 1000 µM XEN445 inhibitor. **b)** Quantification of all populations found on PAP3 liposomal formulation incubating with LPL for 120 min after addition of 1000 µM XEN445 inhibitor. Quantification based on cryo-TEM particle count (N=200).

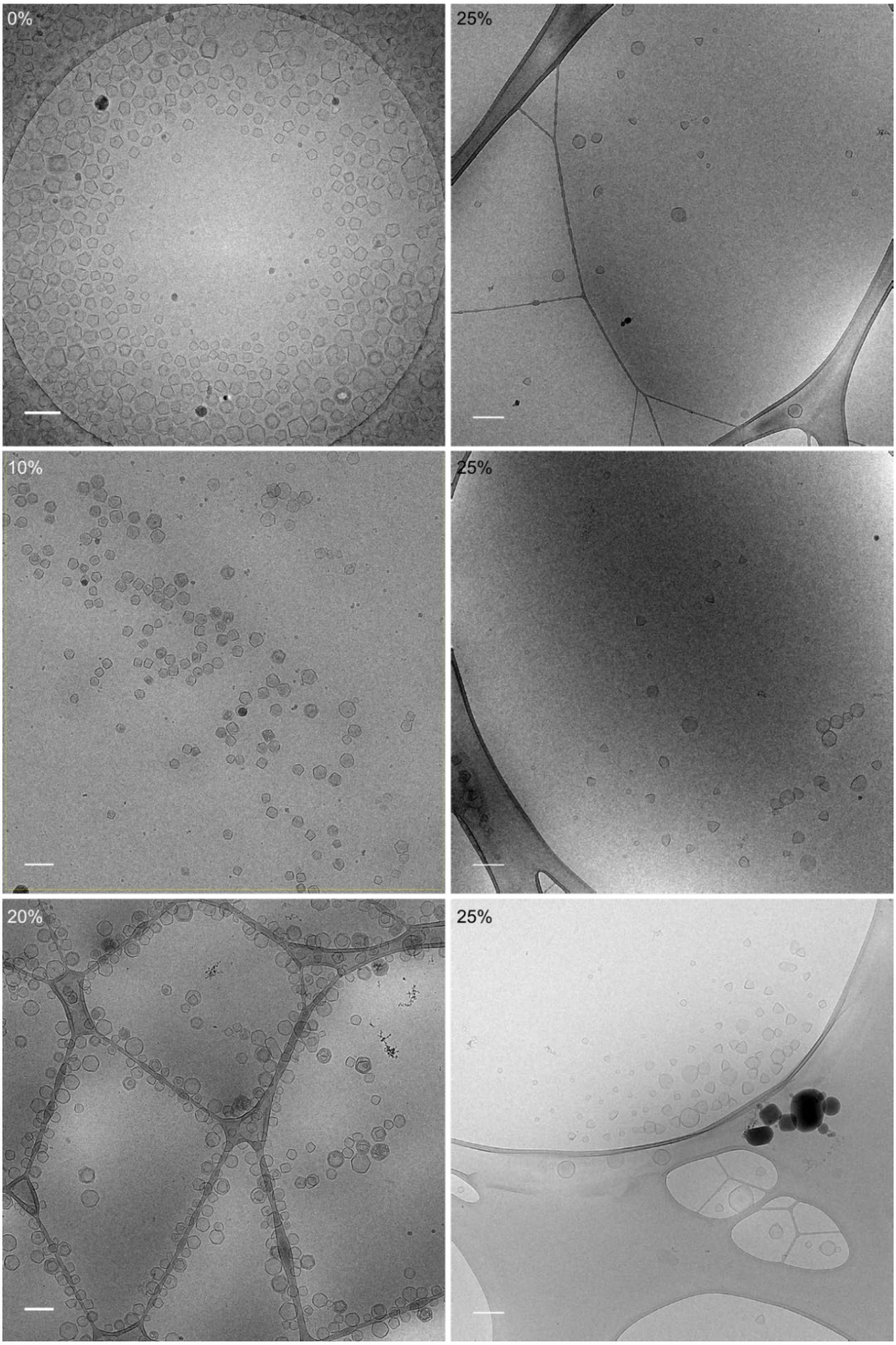
0%
25%
10%
25%
20%
25%

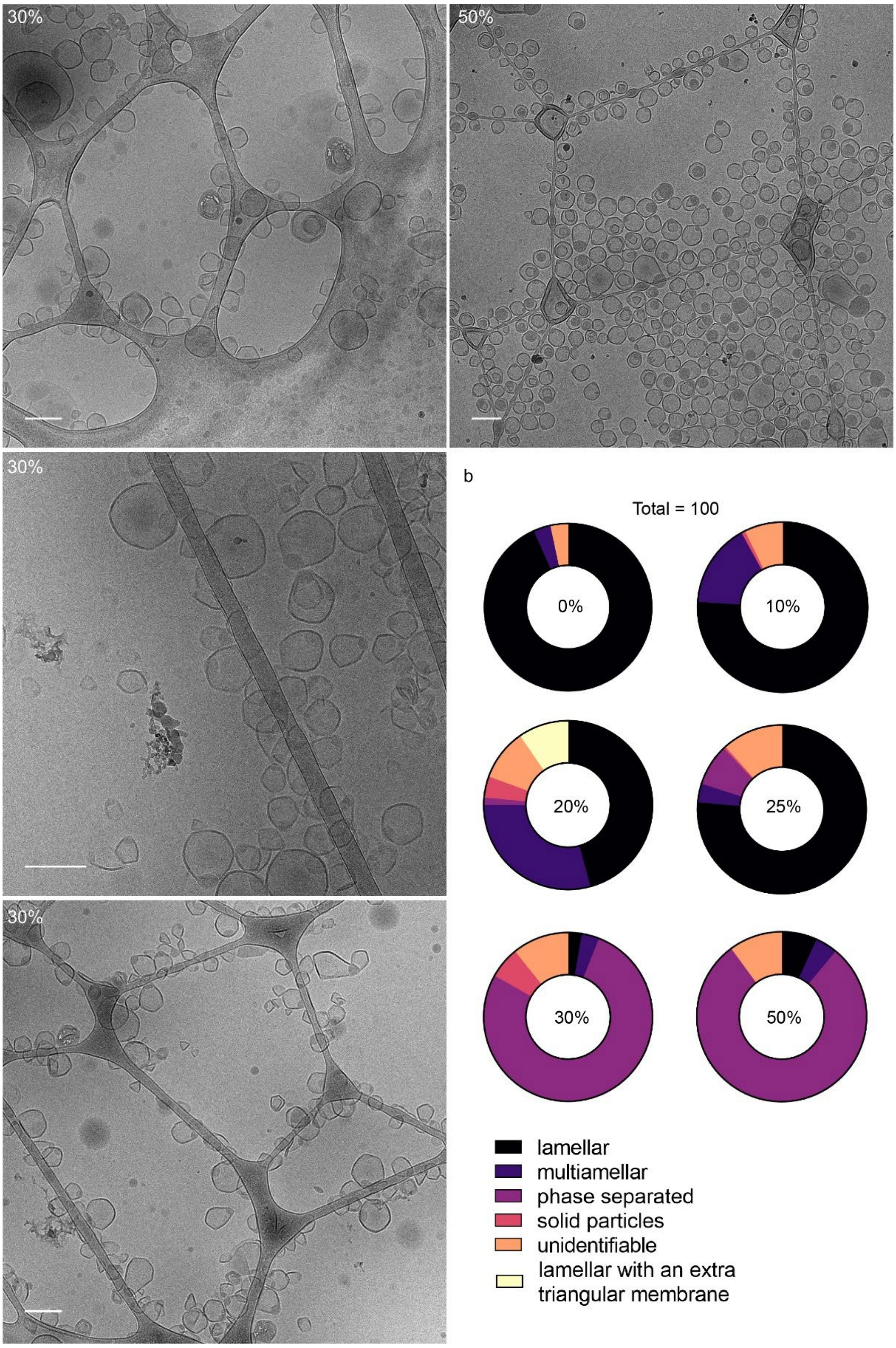

Figure S10. Cryo-TEM images and quantification of PAP3 liposomes formulated at varying molar ratios. a) Cryo-TEM images of liposomes composed of DSPC and 0, 20, 25, 30 and 50 mol % DOaG. Images as chosen for quantification of the whole population. Scale bars: 200 nm. **b)** Quantification of the whole population of liposomes composed of DSPC and 0, 20, 25, 30 and 50 mol % DOaG. Total of each circle chart = 100.

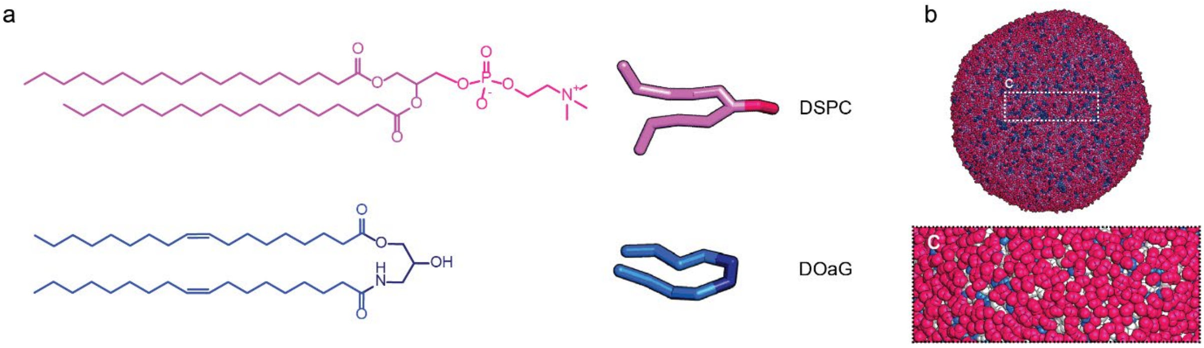

Figure S11. Lipids used for the coarse-grained representation of PAP3 liposomes. a) Molecular structures of DSPC and DOaG lipids and simulated representations. **b)** Modeled lipid droplet of PAP3 liposomes. **c)** Zoom in of b showing the lipid packing defects and the high spacing between DSPC headgroups exposing the DOaG (grey/blue). Size of droplet radius 20.1 nm.

SI 12 Coarse-Grained model

While several lipids have been parametrised within the Martini context, including DSPC, a representation of DOaG is lacking and should be parametrised. Our starting point is an existing representation for a diacylglycerol lipid (DOG), which is very similar to DOaG. Observations by cryo-EM are used as a reference, and indicate that phase separated liposomes are formed for mixtures containing > 25 mol % of DOaG, assuming that DOaG is evenly distributed over all liposomes. The ambiguity in the CG representation of DOaG is in the choice of the head beads, i.e. in the non-bonded interactions that are usually estimated from relative partitioning in two different solvents, and we may use the experimental data for phase separation as an alternative. To quantify phase separation *in silico*, the contact fraction between DOaG and DSPC is used:

$$f_{DOaG-DSPC} = \frac{c_{DOaG-DMPC}}{c_{DOaG-DMPC} + c_{DOaG-DOaG}} \times \frac{1}{\phi_{DOaG}}$$

with c_{i-j} representing the number of contacts between two lipid species, and ϕ_{DOaG} the fraction of DOaG lipids. The normalisation by the DOaG fraction, which is not used in the original formulation[1], is introduced to enable a direct comparison of membranes with different fractions of DOaG, i.e by normalizing the maximum of the contact fraction to unity. To determine if two lipids are in direct contact, the standard distance threshold of 1.1 nm was used for the GL1 bead (if the lipid is a DSPC lipid) and the GLA bead (in case of DOaG). Density profiles, see **Figure S13**, along the membrane normal indicate that these beads reside roughly at the same depth within the monolayer.

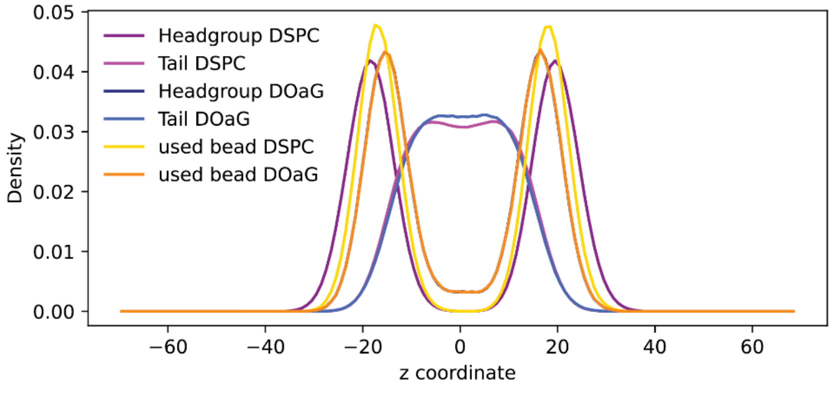

Figure S13. Density profiles of selected bead types across the membrane (along the normal). The contact fraction was subsequently employed to monitor the degree of phase separation for varying DOaG fractions and for different bead-type representations of the DOaG head group in CG Martini. We considered both Martini 2 and 3. Based on the best fit to the experimental data, the DOaG representation with N6a and N6d beads was selected as most appropriate. DPPC = DSPC

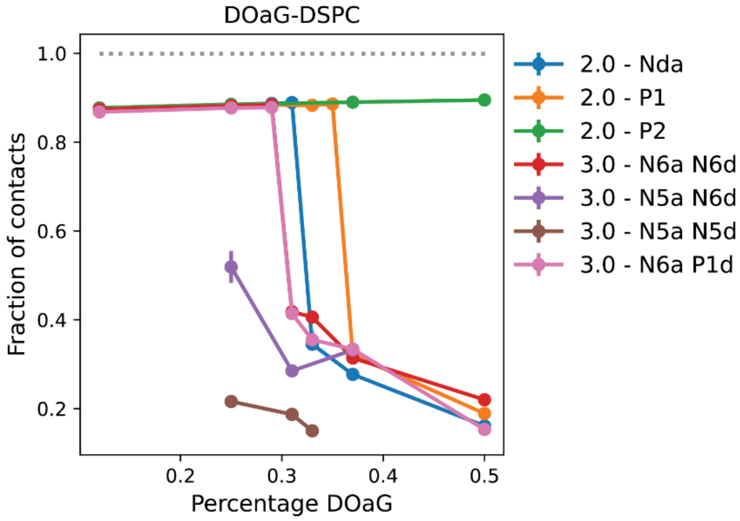

Figure S14. Fractions of contact for increasing composition fractions of DOaG as calculated from CG membrane simulations. Contact fractions have been determined by averaging over the last µs of a 2 µs simulation trajectory.

SI 15. Input file for the CG Martini representation for DOaG used in this study:

```
[moleculetype]; molname      nrexcl
  DOAG         1

[atoms]; id        type      resnr     residu    atom     cgnr
   1      N6a        1       DOAG GLA      1         0
   2      N6d        1       DOAG NAB      2         0
   3      C1         1       DOAG C1A      3         0
   4      C4h        1       DOAG D2A      4         0
   5      C1         1       DOAG C3A      5         0
   6      C1         1       DOAG C4A      6         0
   7      C1         1       DOAG C1B      7         0
   8      C4h        1       DOAG D2B      8         0
   9      C1         1       DOAG C3B      9         0
  10      C1         1       DOAG C4B     10         0

[bonds];
i         j          funct     length    force.c.
   1  2              1         0.312     2500
   1  3              1         0.47      5000
   3  4              1         0.47      3800
   4  5              1         0.47      3800
   5  6              1         0.47      3800
   2  7              1         0.47      3600
   7  8              1         0.47      3800
   8  9              1         0.47      3800
   9 10              1         0.47      3800

[angles];
    i  j  k          funct     angle     force.c.
   1  3  4           2         180.0     35.0
   3  4  5           2         120.0     35.0
   4  5  6           2         180.0     35.0
   2  7  8           2         180.0     35.0
   7  8  9           2         120.0     35.0
   8  9 10           2         180.0     35.0
```

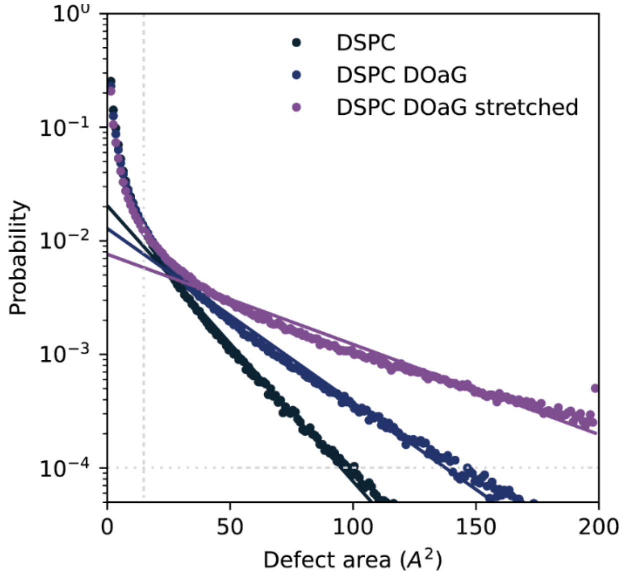

Figure S16. Standard practice when using PackMem is retrieving the packing defect constant from fitting the probability to find a defect of a certain area. This probability of finding a defect of a certain area is given by the formula: $P(A) = b\, e^{-\frac{A}{\pi}}$, where P(A) is the probability of finding a defect area of area A^2, b is a constant and π is the packing defect constant. The fit is performed on all datapoints where the area of the defect is bigger than 15 A^2 and the probability is higher than $1e^{-4}$. The fit for the flat DSPC, flat but phase-separated DSPC/DOaG layer and for the stretched phase-separated DSPC/DOaG layer, are shown in this figure. The solid line of the same color is the fit through the data, which gives the packing defect constant for each system.

SI 17 Identifying lipid packing defect sensing motifs on LPL protein structure

Our previously developed neural network (NN) model is able to predict the relative free energy of a peptide binding to a stretched membrane (high packing defect constant) versus a tensionless membrane (low packing defect constant)[2], only requiring the amino acid sequence. To identify putative regions with lipid packing defect sensing ability within a 3D protein structure of LPL, we used a python script that employs a sliding window of length 15 to screen the protein sequence and predict ΔΔF for every segment. Since the segments overlap, every individual residue is part of more than one segment (except for the termini). By taking the average of these overlapping segment scores at every position we obtained a "per-residue" ΔΔF which can be interpreted as the contribution of that single amino acid to the overall lipid packing defect sensing ability of the respective protein region (Figure S18a).

For a residue to bind to a membrane's lipid packing defects, it must be located at the outer shell of the protein structure, *i.e.,* it must be exposed to the solvent. We accounted for this by calculating the solvent-accessible surface area (SASA) for every individual residue (using BioPython[3]), based on the 3D protein structure. Then, we calculated the average SASA of the direct vicinity: a 9 amino acid stretch ($n_{-4} – n_{+4}$) around the respective residue at position n (Figure S18b). If this averaged SASA exceeded a threshold value of 0.8 nm^2, we considered that residue to be sufficiently solvent exposed to potentially contribute to lipid packing defect sensing ability. If not, that residue was labeled inactive.

By taking both the averaged per-residue ΔΔF and SASA values into account, we mapped and color-coded the predicted lipid packing defect sensing ability onto the 3D protein structure, as we show in

Figure 5b in the main text. For this, we used the B-factor field in the PDB file, applying the following rules:

$$
\begin{aligned}
&if\ SASA < 0.8: \qquad && Bfactor = 0.0 \\
&if\ SASA \geq 0.8: \qquad && Bfactor = \frac{x - x_{max}}{x_{min} - x_{max}} \times 100
\end{aligned}
$$

In which x is the per-residue ΔΔF score and x_{max} and x_{min} are the maximal and minimal value of x for the entire protein. This formula yields a maximal B-factor of 100.0 for the highest score (most negative ΔΔF , $x=x_{min}$) and the minimal B-factor of 0.0 for the lowest score ($x=x_{max}$). Note that ΔΔF values are always negative.

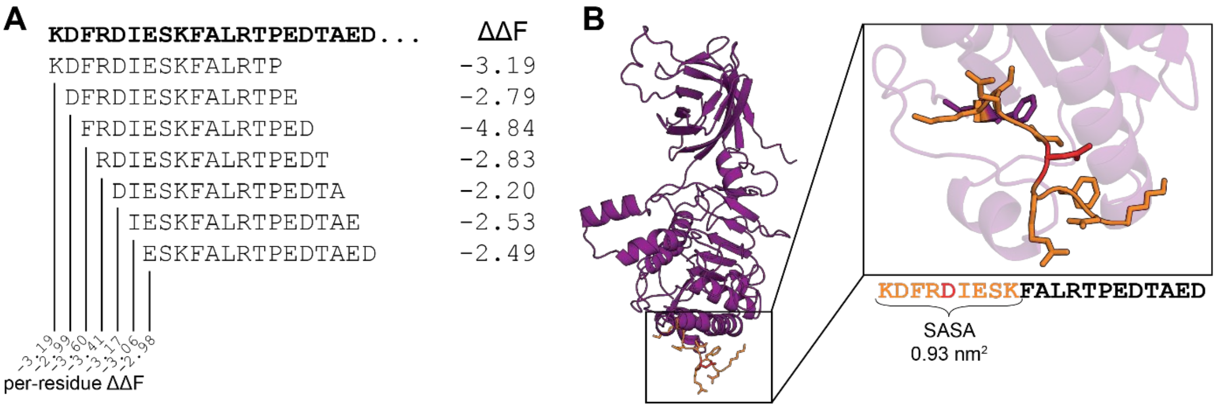

Figure S18. a) An example of NN-predicted ΔΔF values for overlapping 15-residue fragments of LPL (*Bos Taurus*) N-terminal region. The average of the overlapping scores yields the per-residue ΔΔF at every position. **b)** For every amino acid in the 3D protein structure, the individual SASA is calculated. Then, for every position, we compute the average SASA of the 9-residue vicinity (in orange) and assign that value (0.93 nm^2 in this case) to the middle residue (Asp39 in this example, in red).

S19 Residue scores. Per-residue SASA, ΔΔF, and resulting B-factors for LPL (*Bos Taurus*).

		SASA	ΔΔF	B-factor
35	K	1.20	-3.19	22.20
36	D	1.05	-2.99	17.42
37	F	1.04	-3.60	31.98
38	R	0.92	-3.41	27.45
39	D	0.93	-3.17	21.72
40	I	0.73	-3.06	0.00
41	E	0.64	-2.98	0.00
42	S	0.61	-3.00	0.00
43	K	0.39	-3.00	0.00
44	F	0.34	-3.06	0.00
45	A	0.39	-3.00	0.00
46	L	0.46	-3.05	0.00
47	R	0.50	-3.05	0.00
48	T	0.42	-3.06	0.00
49	P	0.47	-3.08	0.00
50	E	0.59	-3.08	0.00
51	D	0.62	-3.09	0.00
52	T	0.73	-2.94	0.00
53	A	0.71	-2.97	0.00
54	E	0.70	-3.05	0.00
55	D	0.52	-3.10	0.00
56	T	0.56	-3.16	0.00
57	C	0.55	-3.20	0.00
58	H	0.55	-3.29	0.00
59	L	0.49	-3.41	0.00
60	I	0.50	-3.46	0.00
61	P	0.51	-3.51	0.00
62	G	0.48	-3.45	0.00
63	V	0.42	-3.45	0.00
64	T	0.49	-3.37	0.00
65	E	0.52	-3.44	0.00
66	S	0.51	-3.44	0.00
67	V	0.63	-3.51	0.00
68	A	0.59	-3.61	0.00
69	N	0.60	-3.78	0.00
70	C	0.57	-3.91	0.00
71	H	0.68	-4.06	0.00
72	F	0.70	-4.17	0.00
73	N	0.69	-4.15	0.00
74	H	0.57	-4.05	0.00
75	S	0.56	-4.16	0.00
76	S	0.39	-4.21	0.00
77	K	0.37	-4.42	0.00
78	T	0.31	-4.55	0.00
79	F	0.23	-4.73	0.00
80	V	0.11	-4.77	0.00
81	V	0.18	-4.86	0.00
82	I	0.11	-4.88	0.00
83	H	0.20	-4.76	0.00
84	G	0.30	-4.64	0.00
85	W	0.32	-4.57	0.00
86	T	0.45	-4.49	0.00
87	V	0.53	-4.44	0.00
88	T	0.56	-4.54	0.00
89	G	0.62	-4.77	0.00

		SASA	ΔΔF	B-factor
90	M	0.54	-4.92	0.00
91	Y	0.54	-5.02	0.00
92	E	0.48	-5.01	0.00
93	S	0.49	-5.08	0.00
94	W	0.47	-5.05	0.00
95	V	0.33	-5.06	0.00
96	P	0.31	-5.05	0.00
97	K	0.27	-5.05	0.00
98	L	0.20	-5.09	0.00
99	V	0.22	-5.01	0.00
100	A	0.39	-4.94	0.00
101	A	0.41	-4.82	0.00
102	L	0.34	-4.76	0.00
103	Y	0.43	-4.62	0.00
104	K	0.55	-4.35	0.00
105	R	0.52	-4.13	0.00
106	E	0.52	-3.90	0.00
107	P	0.52	-3.82	0.00
108	D	0.50	-3.65	0.00
109	S	0.33	-3.64	0.00
110	N	0.28	-3.61	0.00
111	V	0.27	-3.77	0.00
112	I	0.19	-3.90	0.00
113	V	0.09	-4.01	0.00
114	V	0.15	-4.18	0.00
115	D	0.16	-4.28	0.00
116	W	0.16	-4.47	0.00
117	L	0.26	-4.47	0.00
118	S	0.35	-4.41	0.00
119	R	0.50	-4.40	0.00
120	A	0.52	-4.37	0.00
121	Q	0.59	-4.38	0.00
122	Q	0.64	-4.29	0.00
123	H	0.57	-4.26	0.00
124	Y	0.56	-4.17	0.00
125	P	0.60	-4.04	0.00
126	V	0.59	-3.76	0.00
127	S	0.50	-3.56	0.00
128	A	0.46	-3.48	0.00
129	G	0.48	-3.32	0.00
130	Y	0.41	-3.31	0.00
131	T	0.33	-3.25	0.00
132	K	0.42	-3.43	0.00
133	L	0.42	-3.55	0.00
134	V	0.38	-3.65	0.00
135	G	0.30	-3.76	0.00
136	Q	0.37	-3.92	0.00
137	D	0.26	-4.10	0.00
138	V	0.19	-4.34	0.00
139	A	0.21	-4.57	0.00
140	K	0.23	-4.87	0.00
141	F	0.13	-5.19	0.00
142	M	0.15	-5.34	0.00
143	N	0.24	-5.42	0.00
144	W	0.35	-5.56	0.00

		SASA	ΔΔF	B-factor
145	M	0.33	-5.62	0.00
146	A	0.48	-5.54	0.00
147	D	0.48	-5.46	0.00
148	E	0.53	-5.45	0.00
149	F	0.52	-5.70	0.00
150	N	0.57	-5.73	0.00
151	Y	0.60	-5.77	0.00
152	P	0.51	-5.71	0.00
153	L	0.42	-5.62	0.00
154	G	0.36	-5.46	0.00
155	N	0.22	-5.28	0.00
156	V	0.21	-5.27	0.00
157	H	0.15	-5.26	0.00
158	L	0.15	-5.31	0.00
159	L	0.10	-5.37	0.00
160	G	0.04	-5.37	0.00
161	Y	0.04	-5.55	0.00
162	S	0.02	-5.55	0.00
163	L	0.02	-5.58	0.00
164	G	0.02	-5.29	0.00
165	A	0.02	-5.15	0.00
166	H	0.02	-4.90	0.00
167	A	0.01	-4.78	0.00
168	A	0.02	-4.59	0.00
169	G	0.09	-4.47	0.00
170	I	0.17	-4.38	0.00
171	A	0.20	-4.08	0.00
172	G	0.31	-3.93	0.00
173	S	0.47	-3.70	0.00
174	L	0.57	-3.53	0.00
175	T	0.56	-3.33	0.00
176	N	0.61	-3.10	0.00
177	K	0.61	-2.92	0.00
178	K	0.54	-2.82	0.00
179	V	0.45	-2.72	0.00
180	N	0.43	-2.76	0.00
181	R	0.32	-2.84	0.00
182	I	0.16	-2.90	0.00
183	T	0.06	-2.93	0.00
184	G	0.06	-3.10	0.00
185	L	0.01	-3.19	0.00
186	D	0.04	-3.36	0.00
187	P	0.15	-3.50	0.00
188	A	0.15	-3.63	0.00
189	G	0.17	-3.70	0.00
190	P	0.34	-3.80	0.00
191	N	0.36	-3.81	0.00
192	F	0.52	-3.95	0.00
193	E	0.55	-3.89	0.00
194	Y	0.66	-3.94	0.00
195	A	0.66	-3.83	0.00
196	E	0.59	-3.73	0.00
197	A	0.58	-3.67	0.00
198	P	0.57	-3.63	0.00
199	S	0.45	-3.46	0.00

		SASA	ΔΔF	B-factor
200	R	0.56	-3.33	0.00
201	L	0.41	-3.22	0.00
202	S	0.37	-3.04	0.00
203	P	0.33	-2.94	0.00
204	D	0.29	-2.85	0.00
205	D	0.26	-2.75	0.00
206	A	0.27	-2.95	0.00
207	D	0.27	-2.95	0.00
208	F	0.22	-3.11	0.00
209	V	0.10	-3.10	0.00
210	D	0.09	-3.19	0.00
211	V	0.11	-3.26	0.00
212	L	0.06	-3.36	0.00
213	H	0.25	-3.38	0.00
214	T	0.30	-3.41	0.00
215	F	0.35	-3.45	0.00
216	T	0.43	-3.40	0.00
217	R	0.44	-3.38	0.00
218	G	0.67	-3.34	0.00
219	S	0.67	-3.34	0.00
220	P	0.72	-3.32	0.00
221	G	0.71	-3.13	0.00
222	R	0.51	-2.96	0.00
223	S	0.51	-2.91	0.00
224	I	0.52	-2.99	0.00
225	G	0.49	-2.98	0.00
226	I	0.47	-3.05	0.00
227	Q	0.25	-3.03	0.00
228	K	0.26	-3.17	0.00
229	P	0.19	-3.24	0.00
230	V	0.19	-3.28	0.00
231	G	0.19	-3.35	0.00
232	H	0.15	-3.42	0.00
233	V	0.08	-3.45	0.00
234	D	0.06	-3.57	0.00
235	I	0.07	-3.70	0.00
236	Y	0.07	-3.77	0.00
237	P	0.10	-3.82	0.00
238	N	0.16	-3.85	0.00
239	G	0.16	-3.79	0.00
240	G	0.21	-3.77	0.00
241	T	0.25	-3.79	0.00
242	F	0.26	-3.92	0.00
243	Q	0.32	-3.94	0.00
244	P	0.46	-3.96	0.00
245	G	0.51	-3.99	0.00
246	C	0.53	-4.01	0.00
247	N	0.48	-4.05	0.00
248	I	0.60	-4.06	0.00
249	G	0.67	-3.99	0.00
250	E	0.68	-3.86	0.00
251	A	0.73	-3.82	0.00
252	L	0.73	-3.82	0.00
253	R	0.72	-3.73	0.00
254	V	0.87	-3.72	34.84

		SASA	ΔΔF	B-factor
255	I	0.84	-3.66	33.41
256	A	0.98	-3.49	29.36
257	E	0.96	-3.27	24.11
258	R	0.93	-3.10	20.05
259	G	0.95	-2.97	16.95
260	L	0.98	-2.94	16.23
261	G	1.00	-2.83	13.60
262	D	0.92	-2.70	10.50
263	V	0.79	-2.65	0.00
264	D	0.79	-2.59	0.00
265	Q	0.68	-2.69	0.00
266	L	0.58	-2.69	0.00
267	V	0.51	-2.67	0.00
268	K	0.46	-2.67	0.00
269	C	0.38	-2.72	0.00
270	S	0.27	-2.81	0.00
271	H	0.22	-2.93	0.00
272	E	0.17	-3.00	0.00
273	R	0.13	-3.09	0.00
274	S	0.09	-3.23	0.00
275	V	0.10	-3.34	0.00
276	H	0.10	-3.48	0.00
277	L	0.08	-3.68	0.00
278	F	0.08	-3.78	0.00
279	I	0.15	-3.79	0.00
280	D	0.21	-3.72	0.00
281	S	0.28	-3.67	0.00
282	L	0.47	-3.70	0.00
283	L	0.57	-3.69	0.00
284	N	0.59	-3.56	0.00
285	E	0.59	-3.48	0.00
286	E	0.65	-3.47	0.00
287	N	0.64	-3.47	0.00
288	P	0.56	-3.44	0.00
289	S	0.62	-3.31	0.00
290	K	0.53	-3.17	0.00
291	A	0.51	-3.11	0.00
292	Y	0.44	-2.99	0.00
293	R	0.50	-2.95	0.00
294	C	0.59	-2.88	0.00
295	N	0.55	-2.86	0.00
296	S	0.55	-2.89	0.00
297	K	0.64	-2.84	0.00
298	E	0.65	-2.87	0.00
299	A	0.63	-2.94	0.00
300	F	0.58	-2.96	0.00
301	E	0.57	-2.88	0.00
302	K	0.49	-2.91	0.00
303	G	0.42	-2.88	0.00
304	L	0.43	-2.96	0.00
305	C	0.59	-2.92	0.00
306	L	0.71	-2.86	0.00
307	S	0.68	-2.80	0.00
308	C	0.81	-2.70	10.50
309	R	0.72	-2.68	0.00

		SASA	ΔΔF	B-factor
310	K	0.70	-2.69	0.00
311	N	0.71	-2.66	0.00
312	R	0.69	-2.61	0.00
313	C	0.65	-2.54	0.00
314	N	0.52	-2.48	0.00
315	N	0.37	-2.42	0.00
316	M	0.29	-2.40	0.00
317	G	0.25	-2.31	0.00
318	Y	0.35	-2.29	0.00
319	E	0.39	-2.26	0.00
320	I	0.53	-2.27	0.00
321	N	0.59	-2.26	0.00
322	K	0.82	-2.26	0.00
323	V	1.01	-2.29	0.72
324	R	1.01	-2.32	1.43
325	A	1.01	-2.35	2.15
326	K	1.00	-2.40	3.34
327	R	0.89	-2.58	7.64
328	S	0.85	-2.64	9.07
329	S	0.69	-2.79	0.00
330	K	0.66	-2.98	0.00
331	M	0.43	-3.26	0.00
332	Y	0.29	-3.37	0.00
333	L	0.29	-3.52	0.00
334	K	0.42	-3.55	0.00
335	T	0.43	-3.73	0.00
336	R	0.51	-3.86	0.00
337	S	0.51	-4.09	0.00
338	Q	0.57	-4.33	0.00
339	M	0.55	-4.62	0.00
340	P	0.57	-4.82	0.00
341	Y	0.50	-4.94	0.00
342	K	0.45	-4.90	0.00
343	V	0.33	-4.98	0.00
344	F	0.24	-5.04	0.00
345	H	0.25	-4.88	0.00
346	Y	0.23	-4.68	0.00
347	Q	0.26	-4.58	0.00
348	V	0.25	-4.47	0.00
349	K	0.25	-4.43	0.00
350	I	0.27	-4.26	0.00
351	H	0.42	-4.20	0.00
352	F	0.53	-4.01	0.00
353	S	0.66	-3.80	0.00
354	G	0.63	-3.50	0.00
355	T	0.72	-3.30	0.00
356	E	0.71	-3.11	0.00
357	S	0.81	-3.07	19.33
358	N	0.91	-2.97	16.95
359	T	0.90	-2.89	15.04
360	Y	0.77	-2.95	0.00
361	T	0.64	-2.93	0.00
362	N	0.55	-2.98	0.00
363	Q	0.48	-2.94	0.00
364	A	0.40	-2.97	0.00

		SASA	**ΔΔF**	**B-factor**
365	F	0.34	-2.98	0.00
366	E	0.26	-2.95	0.00
367	I	0.16	-3.08	0.00
368	S	0.24	-3.18	0.00
369	L	0.32	-3.38	0.00
370	Y	0.36	-3.46	0.00
371	G	0.43	-3.59	0.00
372	T	0.45	-3.52	0.00
373	V	0.54	-3.61	0.00
374	A	0.63	-3.55	0.00
375	E	0.62	-3.56	0.00
376	S	0.71	-3.59	0.00
377	E	0.64	-3.66	0.00
378	N	0.62	-3.80	0.00
379	I	0.59	-3.93	0.00
380	P	0.58	-4.13	0.00
381	F	0.65	-4.38	0.00
382	T	0.54	-4.38	0.00
383	L	0.46	-4.44	0.00
384	P	0.46	-4.39	0.00
385	E	0.44	-4.32	0.00
386	V	0.52	-4.28	0.00
387	S	0.50	-4.30	0.00
388	T	0.53	-4.28	0.00
389	N	0.46	-4.28	0.00
390	K	0.40	-4.32	0.00
391	T	0.42	-4.32	0.00
392	Y	0.42	-4.35	0.00
393	S	0.50	-4.35	0.00
394	F	0.41	-4.39	0.00
395	L	0.44	-4.29	0.00
396	L	0.40	-4.11	0.00
397	Y	0.46	-4.05	0.00
398	T	0.42	-4.03	0.00
399	E	0.44	-4.13	0.00
400	V	0.48	-4.34	0.00
401	D	0.49	-4.59	0.00
402	I	0.47	-4.87	0.00
403	G	0.51	-5.07	0.00
404	E	0.38	-5.33	0.00
405	L	0.40	-5.54	0.00
406	L	0.31	-5.78	0.00
407	M	0.38	-5.89	0.00
408	L	0.35	-5.92	0.00
409	K	0.34	-5.94	0.00
410	L	0.36	-6.15	0.00
411	K	0.44	-6.31	0.00
412	W	0.46	-6.41	0.00
413	I	0.67	-6.45	0.00
414	S	0.74	-6.33	0.00
415	D	0.76	-6.35	0.00
416	S	0.89	-6.16	93.08
417	Y	0.91	-6.11	91.89
418	F	1.00	-6.01	89.50
419	S	1.23	-5.86	85.92
420	W	1.24	-5.72	82.58
421	S	1.31	-5.56	78.76
422	N	1.12	-5.42	75.42
423	W	1.03	-5.26	71.60
424	W	1.03	-5.06	66.83
425	S	0.83	-4.75	59.43
426	S	0.86	-4.54	54.42
427	P	0.71	-4.36	0.00
428	G	0.47	-4.16	0.00
429	F	0.44	-4.11	0.00
430	D	0.30	-3.83	0.00
431	I	0.44	-3.72	0.00
432	G	0.41	-3.51	0.00
433	K	0.41	-3.50	0.00
434	I	0.43	-3.35	0.00
435	R	0.37	-3.19	0.00
436	V	0.42	-3.06	0.00
437	K	0.48	-3.02	0.00
438	A	0.36	-2.96	0.00
439	G	0.42	-3.04	0.00
440	E	0.36	-3.04	0.00
441	T	0.37	-3.08	0.00
442	Q	0.39	-3.12	0.00
443	K	0.38	-3.22	0.00
444	K	0.41	-3.24	0.00
445	V	0.38	-3.37	0.00
446	I	0.49	-3.43	0.00
447	F	0.63	-3.49	0.00
448	C	0.78	-3.34	0.00
449	S	0.74	-3.36	0.00
450	R	0.74	-3.37	0.00
451	E	0.82	-3.57	31.26
452	K	0.82	-3.72	34.84
453	M	0.85	-3.95	40.33
454	S	0.89	-4.05	42.72
455	Y	0.73	-4.18	0.00
456	L	0.61	-4.22	0.00
457	Q	0.51	-4.19	0.00
458	K	0.50	-4.16	0.00
459	G	0.50	-4.20	0.00
460	K	0.43	-4.21	0.00
461	S	0.43	-4.26	0.00
462	P	0.43	-4.34	0.00
463	V	0.44	-4.44	0.00
464	I	0.49	-4.47	0.00
465	F	0.55	-4.57	0.00
466	V	0.51	-4.48	0.00
467	K	0.58	-4.37	0.00
468	C	0.64	-4.25	0.00
469	H	0.61	-4.09	0.00
470	D	0.74	-4.02	0.00
471	K	0.92	-3.97	40.81
472	S	1.08	-4.14	44.87
473	L	1.13	-4.23	47.02
474	N	1.18	-4.24	47.26

		SASA	ΔΔF	B-factor
475	R	1.25	-4.22	46.78
476	K	1.26	-4.18	45.82
477	S	1.35	-3.83	37.47
478	G	1.56	-3.49	29.36

Triacylglycerol lipase

Superfamily abH15 - Burkholderia lipases
Homologous family abH15.02 (Burkholderia cepacia lipase like)
Organism Burkholderia sp.
Sequences 1
Structures 0

Source DB

gi 78063020

Reference Sequence download

```
MAKTMRSRVV AGAVACAMSI APFAGTTVAM TLATTHAAMA ASSPADGYTA TRYPIILVHG LSGTDKYAGV LEYWYGIQED   80
LQQNGATVYV ANLSGFQSDD GPNGRGEQLL AYVKTVLAAT GATKVNLVGH SQGGLTSRYV AAVAPDLVAS VTTIGTPHRG  160
SEFADFVQNV LAYDPTGLSS SVIAAFVNVF GILTSSSHNT NQDALAALQT LTTARAATYN QNYPSAGLGA PGSCQTGAPT  240
ETVGGNTHLL YSWAGTAIQP TLSLFGVTGA TDTSTIPVVD PANALDLSTL ALYGTGTVMI NRSSGQNDGL VSKCSALYGK  320
VLSTSYKWNH LDEINQLLGV RGAYAEDPVA VIRTHANRLK LAGV                                      364
```

Figure S20. Sequence of Triacylglycerol lipase derived from *Burkholderia sp*. Sequence was obtained by the Lipase engineering Database.[4] Sequence does not indicate a Trp-rich domain. BLAST run does not designate significant matches of the protein with any human protein species.

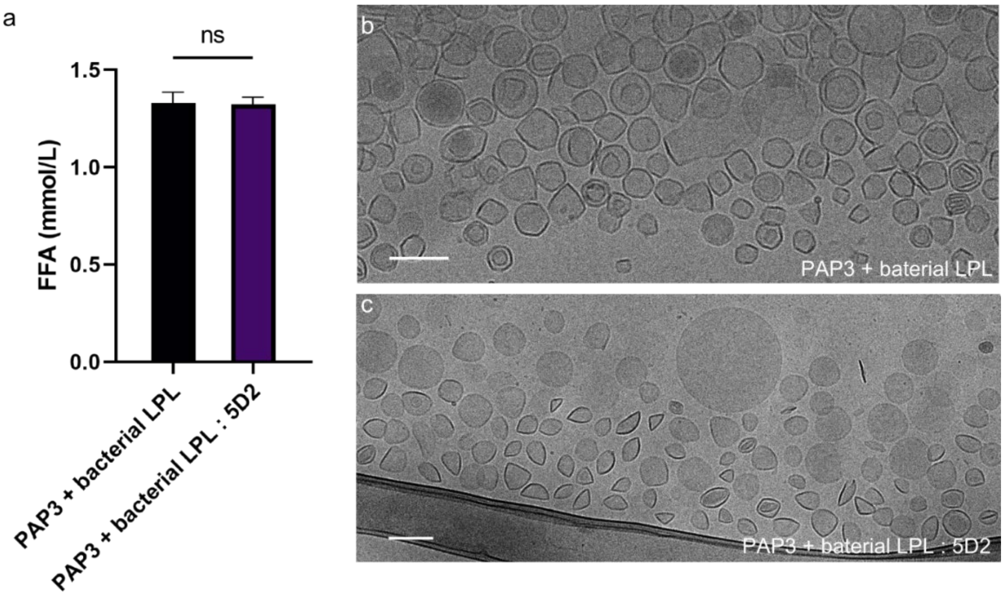

Figure S21. Effect of non-mammalian LPL on PAP3 liposomes with and without 5D2 antibody. a) Release of FFA from PAP3 liposomes incubating at 37 °C with non-mammalian LPL (derived from *Burkholderia sp.*) and non-mammalian LPL + 5D2 antibody (1:1) for 120 min. Cryo-TEM images of PAP3 liposomes after incubating at 37 °C for 120 min with **b)** non-mammalian LPL and **c)** non-mammalian LPL + 5D2 antibody (1:1).

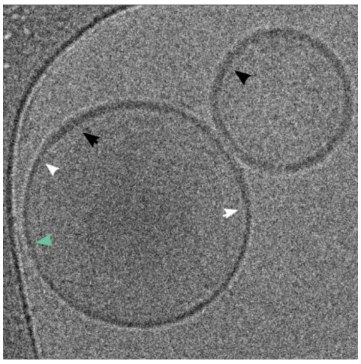

Figure S22. Cryo-TEM image of PAP3 liposomes after incubation with LPL at 37 ºC for 180min. Difference of bilayer thickness is indicated with black (thicker part) or green (thinner part) arrows. The point of thickness mismatch is indicated with white arrows.

```
sp|P11150|LIPC_HUMAN
sp|P06858|LIPL_HUMAN
sp|Q9Y5X9|LIPE_HUMAN

MDTSPLCFSILLVLCIFIQSSALGQSLKPEPFGRRAQA------VETNKTLHEMKTRFLL 54
MESKAL---LVLTLAVWLQSLTAS-RGGV-------------AAADQRRDFIDIESKFAL 43
MSN------SVPLLCFWSLCYCFA-AGSPVPFGPEGRLEDKLHKPKATQTEVKPSVRFNL 53
*..       :  *..:  .   .                     .  :   . . :* *

F---GETNQGCQIRINHPDTLQECGFNSSLPLVMIIHGWSVDGVLENWIWQMVAALKSQP 111
RTPEDTAEDTCHLIPGVAESVATCHFNHSSKTFMVIHGWTVTGMYESWVPKLVAALYKRE 103
RTSKDPEHEGCYLSVGHSQPLEDCSFNMTAKTFFIIHGWTMSGIFENWLHKLVSALHTRE 113
    .  .: * :  .  : :  * ** :   .::****:: *: *.*: ::*:** .:

AQPVNVGLVDWITLAHDHYTIAVRNTRLVGKEVAALLRWLEESVQLSRSHVHLIGYSLGA 171
-PDSNVIVVDWLSRAQEHYPVSAGYTKLVGQDVARFINWMEEEFNYPLDNVHLLGYSLGA 162
-KDANVVVVDWLPLAHQLYTDAVNNTRVVGHSIARMLDWLQEKDDFSLGNVHLIGYSLGA 172
    ** :***:  *:: *  :.  *::**:.:* :: *::*. :   .:***:******

HVSGFAGSSIGGTHKIGRITGLDAAGPLFEGSAPSNRLSPDDANFVDAIHTFTREHMGLS 231
HAAGIAGSLTNK--KVNRITGLDPAGPNFEYAEAPSRLSPDDADFVDVLHTFTRGSPGRS 220
HVAGYAGNFVKG--TVGRITGLDPAGPMFEGADIHKRLSPDDADFVDVLHTYTRS-FGLS 229
*.:* **.      .:.****** *** **  :   .*******:***.:**:**   * *

VGIKQPIGHYDFYPNGGSFQPGCHFLELYRHIAQHGFNAITQTIKCSHERSVHLFIDSLL 291
IGIQKPVGHVDIYPNGGTFQPGCNIGEAIRVIAERGLGDVDQLVKCSHERSIHLFIDSLL 280
IGIQMPVGHIDIYPNGGDFQPGCGLNDVLGSI---AYGTITEVVKCEHERAVHLFVDSLV 286
:**: *:** *:***** ***** : :    *   . . : : :**.***::***:***:

HAGTQSMAYPCGDMNSFSQGLCLSCKKGRCNTLGYHVRQEPRSKSKRLFLVTRAQSPFKV 351
NEENPSKAYRCSSKEAFEKGLCLSCRKNRCNNLGYEINKVRAKRSSKMYLKTRSQMPYKV 340
NQDKPSFAFQCTDSNRFKKGICLSCRKNRCNSIGYNAKKMRNKRNSKMYLKTRAGMPFRV 346
:  . * *: * . : *.:*:****:*.***.:**. .:   .:..:::* **:  *::*

YHYQFKIQFINQ-TETPIQTTFTMSLLGTKEKMQKIPITLGKGIASNKTYSFLITLDVDI 410
FHYQVKIHFSGTESETHTNQAFEISLYGTVAESENIPFTLPE-VSTNKTYSFLIYTEVDI 399
YHYQMKIHVFSYKNMGEIEPTFYVTLYGTNADSQTLPLEIVERIEQNATNTFLVYTEEDL 406
:***.**:. .  .    : :* ::* **  . :.:*: : : :  * * :**:  : *:

GELIMIKFKWENSA--VWANVWDTVQTIIPWSTGPRHSGLVLKTIRVKAGETQQRMTFCS 468
GELLMLKLKWKSDSYFSWSDWWSS-------------PGFAIQKIRVKAGETQKKVIFCS 446
GDLLKIQLTWEGASQ-SWYNLWKEFRSYLSQPRNP-GRELNIRRIRVKSGETQRKLTFCT 464
*:*: :::.*:. :   * : *.                : :: ****:****::: **:

ENTDDLLLRPTQEKIFVKCEIKSKTSKRKIR-----  499
REKVSHLQKGKAPAVFVKCHDKSLNKKSG-------  475
EDPENTSISPGRELWFRKCRDGWRMKNETSPTVELP  500
.:  .          * **.     .:
```

Figure S23. Sequence alignment of Triacylglycerol Lipases Hepatic, Lipoprotein and Endothelial Lipase (*Homo Sapiens*). Sequence alignment was run by an alignment tool provided by Uniprot.org database. Uniprot IDs: P11150 (in magenta), P06858 (in blue) and Q9Y5X9 (in black) respectively. Conserved amino acids indicated with *. Similar amino acids indicated with “ : ” , somewhat similar amino acids indicated with “ . ” . Tryptophan-rich loop indicated in purple box.

```
sp|P11151|LIPL_BOVIN
sp|P06858|LIPL_HUMAN

MESKALLLLALSVCLQSLTVSRGGLVAADRITGGKDFRDIESKFALRTPEDTAEDTCHLI 60
MESKALLVLTLAVWLQSLTASRGGVAAADQ---RRDFIDIESKFALRTPEDTAEDTCHLI 57
*******:*:*:* *****.****:.***:    :** **********************

PGVTESVANCHFNHSSKTFVVIHGWTVTGMYESWVPKLVAALYKREPDSNVIVVDWLSRA 120
PGVAESVATCHFNHSSKTFMVIHGWTVTGMYESWVPKLVAALYKREPDSNVIVVDWLSRA 117
***:****.**********:****************************************

QQHYPVSAGYTKLVGQDVAKFMNWMADEFNYPLGNVHLLGYSLGAHAAGIAGSLTNKKVN 180
QEHYPVSAGYTKLVGQDVARFINWMEEEFNYPLDNVHLLGYSLGAHAAGIAGSLTNKKVN 177
*:*****************:*:*** :******.**************************

RITGLDPAGPNFEYAEAPSRLSPDDADFVDVLHTFTRGSPGRSIGIQKPVGHVDIYPNGG 240
RITGLDPAGPNFEYAEAPSRLSPDDADFVDVLHTFTRGSPGRSIGIQKPVGHVDIYPNGG 237
************************************************************

TFQPGCNIGEALRVIAERGLGDVDQLVKCSHERSVHLFIDSLLNEENPSKAYRCNSKEAF 300
TFQPGCNIGEAIRVIAERGLGDVDQLVKCSHERSIHLFIDSLLNEENPSKAYRCSSKEAF 297
***********:**********************:*******************.*****

EKGLCLSCRKNRCNNMGYEINKVRAKRSSKMYLKTRSQMPYKVFHYQVKIHFSGTESNTY 360
EKGLCLSCRKNRCNNLGYEINKVRAKRSSKMYLKTRSQMPYKVFHYQVKIHFSGTESETH 357
***************:*****************************************:*:

TNQAFEISLYGTVAESENIPFTLPEVSTNKTYSFLLYTEVDIGELLMLKLKWISDSYFSW 420
TNQAFEISLYGTVAESENIPFTLPEVSTNKTYSFLIYTEVDIGELLMLKLKWKSDSYFSW 417
***********************************:**************** *******

SNWWSSPGFDIGKIRVKAGETQKKVIFCSREKMSYLQKGKSPVIFVKCHDKSLNRKSG   478
SDWWSSPGFAIQKIRVKAGETQKKVIFCSREKVSHLQKGKAPAVFVKCHDKSLNKKSG   475
*:******* * ********************:*:*****:*.:**********:***
```

Figure S24. Sequence alignment of LPL derived from *Bos Taurus* (bovine) and *Homo Sapiens* (Human). Sequence alignment was run by an alignment tool provided by Uniprot.org database showing 92.21% homology. Uniprot IDs: P11151 for Bovine LPL (in blue) and P06858 for Human LPL (in black). Conserved amino acids indicated with *. Similar amino acids indicated with " **:** " , somewhat similar amino acids indicated with "**.** " . Tryptophan-rich loop indicated in purple box.

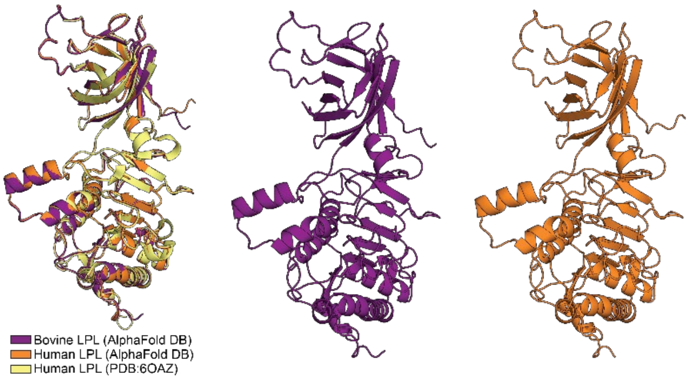

Figure S25. AlphaFold and X-ray protein structures overlap. The AlphaFold DB[5,6] models of bovine and human LPL closely overlap with the human LPL crystal structure (PDB: 60AZ)[7].

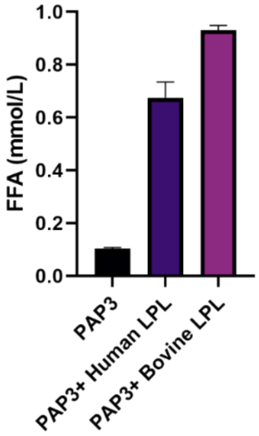

Figure S26. Release of FFA from PAP3 liposomes incubating with Human LPL and Bovine LPL. PAP3 liposomes incubating at 37 °C with LPL for 120 min.

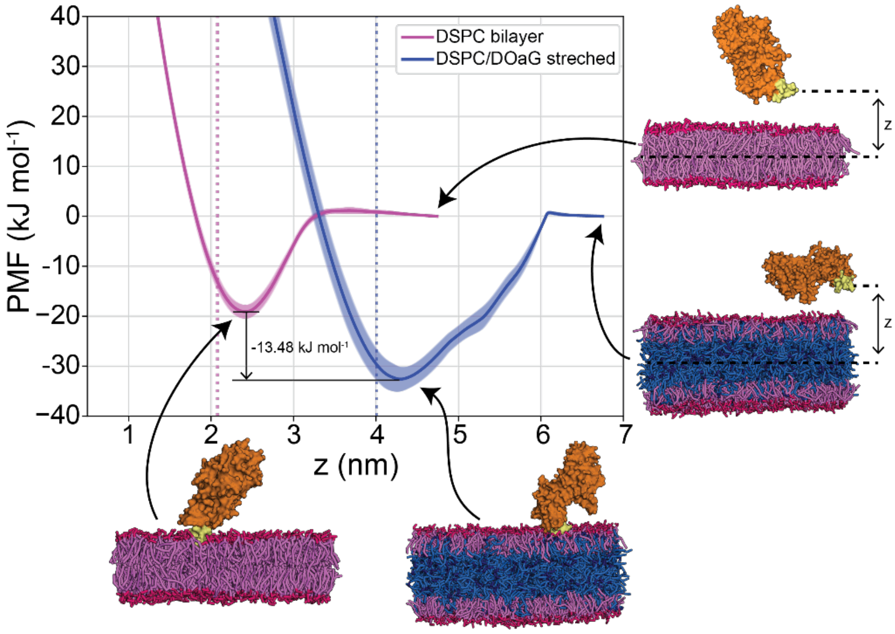

Figure S27. Potential of mean force (PMF) profiles of human LPL binding to a DSPC bilayer (in red-pink) and a DSPC/DOaG phase separated membrane (in red-pink/blue). The US reaction coordinate is the z-distance between the COM of the Trp-rich loop (in yellow) and the COM of the lipids (i.e. center plane of the membrane). Snapshots are the final frames of the trajectories and indicate that the protein is completely unbound at high z (free energy = 0 kJ mol^{-1}) and membrane-bound through the Trp-rich loop at the minima. Dotted lines indicate the position of the DSPC head groups (NC3 beads).

Materials and Methods

General reagents

1,2-distearoyl-*sn*-glycero-3-phosphatidylcholine (DSPC), was purchased from Avanti Polar Lipids (Alabaster, AL, US). Additional DSPC was purchased from Lipoid GmbH. XEN445, Lipoprotein Lipase derived from Bovine milk and Lipoprotein Lipase derived from *Burkholderia Sp.* was purchased from Sigma Aldrich. Human LPL (recombinant derived from CHO cells) was purchased from R&D systems, Bio-techne. Non-Esterified Fatty Acid measurement kit (NEFA-HR2, FUJIFILM Wako chemicals) was purchased from Sopachem, the Netherlands. Anti-lipoprotein lipase monoclonal antibody - 5D2 clone and negative IgG isotype control - was purchased from Biorad, United Kingdom. All other chemical reagents were purchased at the highest grade available from Sigma Aldrich and used without further purification. All solvents were purchased from Biosolve Ltd. Ultrapure MilliQ® water, purified by a MilliQ Advantage A10 water purification system from MilliPore, was used throughout.

Synthesis of DOaG and DOG lipids

DOaG and DOG lipids were synthesized as previously reported[8] and isolated as regioisomeric mixtures: 80% isomer where acyl chains substituting the sn-1 and sn-3 positions of the backbone and 20% isomer where acyl chains substituting the sn-1 and sn-2 positions of the backbone) :

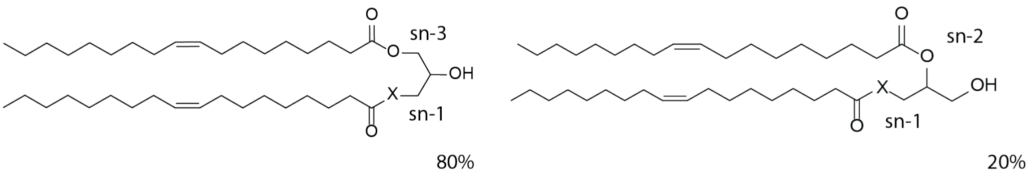

where X = O or N

Lipoprotein Lipase

Lipoprotein Lipase (from bovine milk, Sigma-Aldrich) in ammonium sulfate suspension was centrifuged in a low protein binding tube (DNA Lobind, Eppendorf) for 15 min at 15.000 g (at 4 ºC) and the supernatant was removed. The precipitate was then dissolved gently in Tris Buffer 10mM, pH 7.4 and spun again for 15 min at 15.000 g. The supernatant containing the dissolved protein was then kept and concentrated with spin filtration (Amicon, MWCO 10 kDa). The new concentration was determined using a NanoDrop™ One/One^{C} Microvolume UV-Vis Spectrophotometer (Thermo Scientific) according to Lambert's beer equation ($A = \varepsilon\ b\ c$) with an extinction coefficient $\varepsilon = 71040$ L/moL.

To ensure retrieval of all LPL from the manufacture's bottle, any leftover precipitate in the bottle was dissolved in Tris Buffer (10 mM, pH = 7.4) and dialyzed against the same buffer to remove residual ammonium sulfate. The solution was then centrifuged at 15000 g for 15 min and the supernatant was kept, concentrated and concentration was determined as stated above. LPL was then aliquoted in low protein binding tubes (DNA Lobind, Eppendorf) and kept at -80 ºC until usage.

Lipoprotein Lipase (Human, derived from CHO cells) was firstly dialyzed against Tris Buffer 10 mM pH = 7.4 and then concentrated. The new concentration was determined as described above. Similarly, it was kept at -80 ºC aliquoted for further use.

Inactivation of LPL

Lipase in Tris Buffer (10mM, pH=7.4) was added in a low protein binding tube (DNA LoBind, Eppendorf) and heated up to 95 °C for 10 min in a thermomixer (Eppendorf) to ensure denaturation.

Inhibition of LPL by XEN445 inhibitor

To inhibit the catalytic activity of LPL before incubation with PAP3 liposomes, the lipase was incubated for 30 min at room temperature with the TGL inhibitor XEN445 at different concentrations (titration). The inhibitor was freshly dissolved in DMSO as a stock solution of 10 mM and subsequently added to a low-protein binding Eppendorf tube (DNA-LoBind) containing LPL, to reach final concentration of 0, 50, 100, 500 or 1000 µM and at a constant DMSO content of 5% v/v. LPL concentration was so that it would reach 0.03 mg/mL final concentration after incubation with liposomes, as stated previously.

Cryo-TEM Quantification

Software Fiji (ImageJ) was used for image processing and quantification. Individual low magnification images (up to 3 images per sample) were used to provide a big population of at least 200 nanoparticles. Particles were then counted and divided into categories (lamellar, multilamellar, phase separated, solid particles), according to their morphology. Liposomes whose morphology was not able to be identified (due to image quality) were marked as "unidentifiable" and the value obtained was used as standard deviation for the rest of population. Liposomes that were seen to be on top or in close contact with the copper grid or overlapping with each other, were excluded from the quantification. Particles consisting of two distinct liposomal cores and one lipid droplet (i.e., sharing the droplet) were quantified as one individual phase-separated particle. For quantification and calculation of the radius of the PAP3 droplet, the area A (nm^2) of each individual droplet (N = 100) was measured by the 2D projection of liposomes as obtained by cryo-TEM imaging. The average droplet radius r (nm) was then calculated from the formula: $A = \pi r^2$.

Mass spectrometry analysis

Analysis of DSPC and DOaG by LC-MS/MS

Solutions of DSPC and DOaG (1 pmol/µL) were prepared in 5 mM ammonium formate, in methanol. The compounds were introduced in the mass spectrometer and the tuning conditions for both compounds were determined as indicated below.

MS/MS parameters

Mass Spectrometer	Xevo TQ-S micro (Waters)
Capillary voltage	3.50 kV
Source temperature	150°C
Desolvation temperature	450°C
Cone gas	50 L/h
Desolvation gas	950 L/h

Compound	Retention time (min)	Parent (m/*z*)	Daughter (m/*z*)	Cone Voltage (V)	Collision energy (V)
DOaG	2.51	620.9	602.9	15	15
DSPC	4.45	790.7	184.0	15	20

Lipid extraction

For the MS analysis and for each time point, 9 µL of each sample (PAP3 liposomes incubating at 37 ºC with or without LPL) was flush frozen in liquid nitrogen to ensure discontinuation of the hydrolysis. Subsequently the samples were extracted by a modified Bligh and Dyer extraction[9] using acidic buffer (100 mM ammonium formate buffer, pH = 3.1). In an Eppendorf tube, 400 µL methanol and 200 µL of chloroform were added to the sample. The sample was vortexed for 30 min at room temperature and centrifuged for 10 min at 15,700 g to spin down precipitated protein. The supernatant was transferred to a new Eppendorf tube and 200 µL chloroform and 350 µL water were added for extraction of the lipids. After centrifugation (5 min at 15,700 g), the lower (organic) phase was transferred to a clean Eppendorf tube and the upper (aqueous) phase was re-extracted by adding 400 µL of chloroform. Organic phases were pooled and taken to dryness at 45 °C under a nitrogen stream. Next, the residue was dissolved in 600 µL of butanol and 600 µL of water, mixed and centrifuged for 10 min at 15,700 g. The butanol phase was transferred to a clean tube and taken to dryness in Eppendorf Concentrator Plus at 45 °C. The residue was dissolved in 100 µL methanol, stirred and sonicated in a bath for 30 s and centrifuged for 10 min at 15,700 × g. Finally, 10 µL of the supernatant was applied to the UPLC-MS/MS. Data are the average of 2 experiments.[10]

LC-MS/MS

Measurements were performed by reverse-phase liquid chromatography using a Waters UPLC-Xevo-TQS micro and a BEH C18 column, 2.1 × 50 mm with 1.7 µm particle size (Waters, USA), by applying an isocratic elution of methanol containing 10 mM ammonium formate. The UPLC program was applied for 7 min at a flow rate of 0.250 mL/min. The temperature of the column and of the autosampler were kept at 23°C and 10°C, respectively, during the run. Data were analyzed with Masslynx 4.2 Software (Waters Corporation; Milford MA).

Liposome characterization

Size and polydispersity measurements

Particle size and polydispersity were measured using a Malvern Zetasizer Nano ZS (operating wavelength = 633 nm). Measurements were carried out at room temperature (25 ºC) or at 37 ºC in Tris Buffer 10 mM, pH = 7.4 and at a total lipid concentration of approx. 100 µM. All reported DLS measurements are the average of three measurements.

Table S1. Physicochemical properties of liposomes

Formulation	Size (nm)	PDI	T	Formulation	Size (nm)	PDI	T
PAP3	± 143.2	0.294	25	PAP3 + LPL:XEN445 0uM	±147.5	0.124	37
PAP3 30 min	± 151.8	0.330	37	PAP3 + LPL:XEN445 50uM	±146.9	0.117	37
PAP3 120 min	± 154.4	0.370	37	PAP3 + LPL:XEN445 100uM	±147.4	0.110	37
PAP3 300 min	± 150.8	0.350	37	PAP3 + LPL:XEN445 500uM	±141.2	0.116	37
PAP3 + LPL 30 min	± 159.5	0.085	37	PAP3 + LPL:XEN445 1000uM	±136.7	0.099	37
PAP3 + LPL 120 min	± 158.5	0.104	37	PAP3 (10% DOaG)	±97.5	0.051	25
PAP3 + LPL 300 min	± 166.0	0.200	37	PAP3 (20% DOaG)	±139.3	0.230	25
PAP3 + inactive LPL 30 min	± 146.3	0.275	37	PAP3 (30% DOaG)	±109.3	0.140	25
PAP3 + inactive LPL 120 min	± 141.5	0.256	37	PAP3 (10% DOaG) + LPL	±106.5	0.072	37
PAP3 + inactive LPL 300 min	± 140.4	0.269	37	PAP3 (20% DOaG) + LPL	±104.5	0.047	37
DSPC	± 135.7	0.344	37	PAP3 (30% DOaG) + LPL	±115.3	0.103	37
DSPC + LPL 30 min	± 142.0	0.265	37	PAP3 + LPL:5D2	±151.8	0.184	37
DSPC + LPL 120 min	± 148.4	0.382	37	PAP3 + LPL:IgG	±158.7	0.182	37
DSPC + LPL 300 min	± 128.1	0.208	37	PAP3 + bacterial LPL	±155.0	0.156	37
Myocet®-like (POPC:CHO_55:45) + LPL	± 114.2	0.065	37	PAP3 + bacterial LPL:5D2	±149.4	0.143	37

References

(1) Liu, Y.; de Vries, A. H.; Pezeshkian, W.; Marrink, S. J. Capturing Membrane Phase Separation by Dual Resolution Molecular Dynamics Simulations. *J. Chem. Theory Comput* **2021**, *17*, 5884.

(2) Hilten, N. van; Methorst, J.; Verwei, N.; Risselada, H. J. Physics-Based Generative Model of Curvature Sensing Peptides; Distinguishing Sensors from Binders. *bioRxiv* **2022**, 2022.09.01.506157.

(3) Cock, P. J. A.; Antao, T.; Chang, J. T.; Chapman, B. A.; Cox, C. J.; Dalke, A.; Friedberg, I.; Hamelryck, T.; Kauff, F.; Wilczynski, B.; de Hoon, M. J. L. Biopython: Freely Available Python Tools for Computational Molecular Biology and Bioinformatics. *Bioinformatics* **2009**, *25* (11), 1422–1423.

(4) Fischer, M.; Pleiss, J. The Lipase Engineering Database: A Navigation and Analysis Tool for Protein Families. *Nucleic Acids Res* **2003**, *31* (1), 319.

(5) Jumper, J.; Evans, R.; Pritzel, A.; Green, T.; Figurnov, M.; Ronneberger, O.; Tunyasuvunakool, K.; Bates, R.; Žídek, A.; Potapenko, A.; Bridgland, A.; Meyer, C.; Kohl, S. A. A.; Ballard, A. J.; Cowie, A.; Romera-Paredes, B.; Nikolov, S.; Jain, R.; Adler, J.; Back, T.; Petersen, S.; Reiman, D.; Clancy, E.; Zielinski, M.; Steinegger, M.; Pacholska, M.; Berghammer, T.; Bodenstein, S.; Silver, D.; Vinyals, O.; Senior, A. W.; Kavukcuoglu, K.; Kohli, P.; Hassabis, D. Highly Accurate Protein Structure Prediction with AlphaFold. *Nature* **2021**, *596* (7873), 583–589.

(6) Method of the Year 2021: Protein Structure Prediction. *Nature methods*. Nature January 11, 2022, p 1.

(7) Arora, R.; Nimonkar, A. v.; Baird, D.; Wang, C.; Chiu, C. H.; Horton, P. A.; Hanrahan, S.; Cubbon, R.; Weldon, S.; Tschantz, W. R.; Mueller, S.; Brunner, R.; Lehr, P.; Meier, P.; Ottl, J.; Voznesensky, A.; Pandey, P.; Smith, T. M.; Stojanovic, A.; Flyer, A.; Benson, T. E.; Romanowski, M. J.; Trauger, J. W. Structure of Lipoprotein Lipase in Complex with GPIHBP1. *Proc Natl Acad Sci U S A* **2019**, *116* (21), 10360–10365.

(8) Arias-Alpizar, G.; Papadopoulou, P.; Rios, X.; Reddy Pulagam, K.; Moradi, M.-A.; Pattipeiluhu, R.; Bussmann, J.; Sommerdijk, N.; Llop, J.; Kros, A.; Campbell, F.; Arias-Alpizar, G.; Papadopoulou, P.; Bussmann, J.; Pattipeiluhu, R.; Kros, A.; Campbell, F.; Chemistry, B.; M-A Moradi, S.; Sommerdijk, N. Phase-Separated Liposomes Hijack Endogenous Lipoprotein Transport and Metabolism Pathways to Target Subsets of Endothelial Cells in Vivo. *Adv Healthc Mater* **2023**, 2202709.

(9) Bligh, E. G.; Dyer, W. J. A Rapid Method of Total Lipid Extraction and Purification. *Can J Biochem Physiol* **1959**, *37* (8), 911–917.